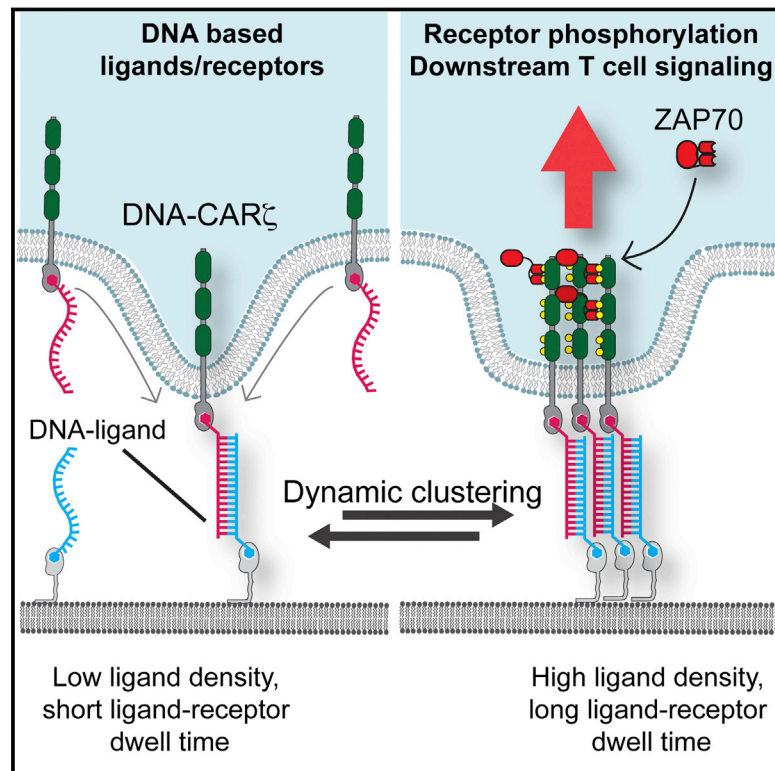# Cell

A DNA-Based T Cell Receptor Reveals a Role for Receptor Clustering in Ligand Discrimination

Graphical Abstract

Authors

Marcus J. Taylor, Kabir Husain,
Zev J. Gartner, Satyajit Mayor,
Ronald D. Vale

Correspondence

mayor@ncbs.res.in (S.M.),
ron.vale@ucsf.edu (R.D.V.)

In Brief

The spatial reorganization of T cell receptors is critical for ligand discrimination in T cell signaling.

Highlights

- A synthetic T cell signaling system was created using receptor ligands made of DNA

- T cell signaling can discriminate between DNA ligands differing by a single base pair

- Higher-affinity ligands promote the clustering and phosphorylation of receptors

- Receptor clustering provides a kinetic proofreading mechanism for ligand discrimination

CellPress

A DNA-Based T Cell Receptor Reveals a Role for Receptor Clustering in Ligand Discrimination

Marcus J. Taylor,[1,3,5] Kabir Husain,[3,4] Zev J. Gartner,[6] Satyajit Mayor,[3,5,*] and Ronald D. Vale[1,2,5,7,*]

[1]Department of Cellular and Molecular Pharmacology
[2]Howard Hughes Medical Institute
University of California San Francisco, San Francisco, CA 94143, USA
[3]National Centre for Biological Sciences, Bangalore 560065, India
[4]The Simons Centre for the Study of Living Machines, Bangalore 560065, India
[5]HHMI Summer Institute, Woods Hole, MA 02543, USA
[6]Department of Pharmaceutical Chemistry, University of California San Francisco, San Francisco, CA 94143, USA
[7]Lead Contact
*Correspondence: mayor@ncbs.res.in (S.M.), ron.vale@ucsf.edu (R.D.V.)
http://dx.doi.org/10.1016/j.cell.2017.03.006

SUMMARY

A T cell mounts an immune response by measuring the binding strength of its T cell receptor (TCR) for peptide-loaded MHCs (pMHC) on an antigen-presenting cell. How T cells convert the lifetime of the extracellular TCR-pMHC interaction into an intracellular signal remains unknown. Here, we developed a synthetic signaling system in which the extracellular domains of the TCR and pMHC were replaced with short hybridizing strands of DNA. Remarkably, T cells can discriminate between DNA ligands differing by a single base pair. Single-molecule imaging reveals that signaling is initiated when single ligand-bound receptors are converted into clusters, a time-dependent process requiring ligands with longer bound times. A computation model reveals that receptor clustering serves a kinetic proofreading function, enabling ligands with longer bound times to have disproportionally greater signaling outputs. These results suggest that spatial reorganization of receptors plays an important role in ligand discrimination in T cell signaling.

INTRODUCTION

The recognition of foreign antigens by T cells begins with a binding interaction between cell-surface peptide-loaded MHC (pMHC) and the T cell receptor (TCR) expressed on the surface of T cells. A pMHC-TCR interaction of sufficient strength triggers the phosphorylation of immunoreceptor tyrosine activation motifs in the TCRζ and associated CD3 chains by the Src family kinase Lck. The mechanism by which pMHC engagement leads to TCR phosphorylation remains controversial; current models include receptor conformational changes (Janeway, 1995) and exclusion of the inhibitory transmembrane phosphatase CD45 from zones of pMHC-TCR engagement (Davis and van der Merwe, 1996). The phosphorylated ITAM domains then recruit

the kinase ZAP70, which in turn phosphorylates the adaptor protein LAT (linker for activation of T cells). Downstream of LAT, numerous signaling pathways become activated, including the MAP kinase pathway, actin polymerization, elevation of intracellular calcium, and large-scale changes in transcription (Brownlie and Zamoyska, 2013).

A remarkable feature of T cells is their ability to respond to and clear the body of viral and microbial infection but not mount a destructive response to the body's own cells. Through genetic recombination, each T cell expresses a unique TCR with its own binding specificity. Unlike many cell-surface receptors that interact with a single or limited number of ligands, the TCR is presented with an immense number of different peptides loaded onto MHC molecules. The vast majority of these peptides are low-affinity antigens derived from the body's own cells. In order not to generate a harmful auto-immune response, mature T cells must ignore the majority of these low-affinity interactions and selectively activate in response to pMHC loaded with higher-affinity foreign peptides.

Previous studies have implicated the lifetime of the TCR-pMHC interaction as a key determinant that distinguishes activating from non-activating pMHC molecules (Davis et al., 1998; Gascoigne et al., 2001). Remarkably, even a few-fold variation in the off-rates of different peptide-bound MHCs for a given TCR can result in all-or-none differences in downstream signaling outputs at physiological ligand densities (Altan-Bonnet and Germain, 2005). However, a mechanistic explanation of how lifetime of an extracellular interaction is "read out" and then converted to an intracellular signal is not well understood. A theory of "kinetic proofreading" was developed to explain how relatively small differences in receptor-bound time might be discriminated and lead to more binary downstream outputs (McKeithan, 1995). In the general formulation of kinetic proofreading, signaling is triggered by a linked set of reactions that require the continuous occupancy of the ligand-receptor complex; if the ligand dissociates, then these reactions are rapidly reversed and the receptor is reset to an inactive state. Many different molecular mechanisms have been put forth for the kinetic proofreading steps, including enzymatic reactions (e.g., phosphorylation), receptor conformational changes, and receptor dimerization
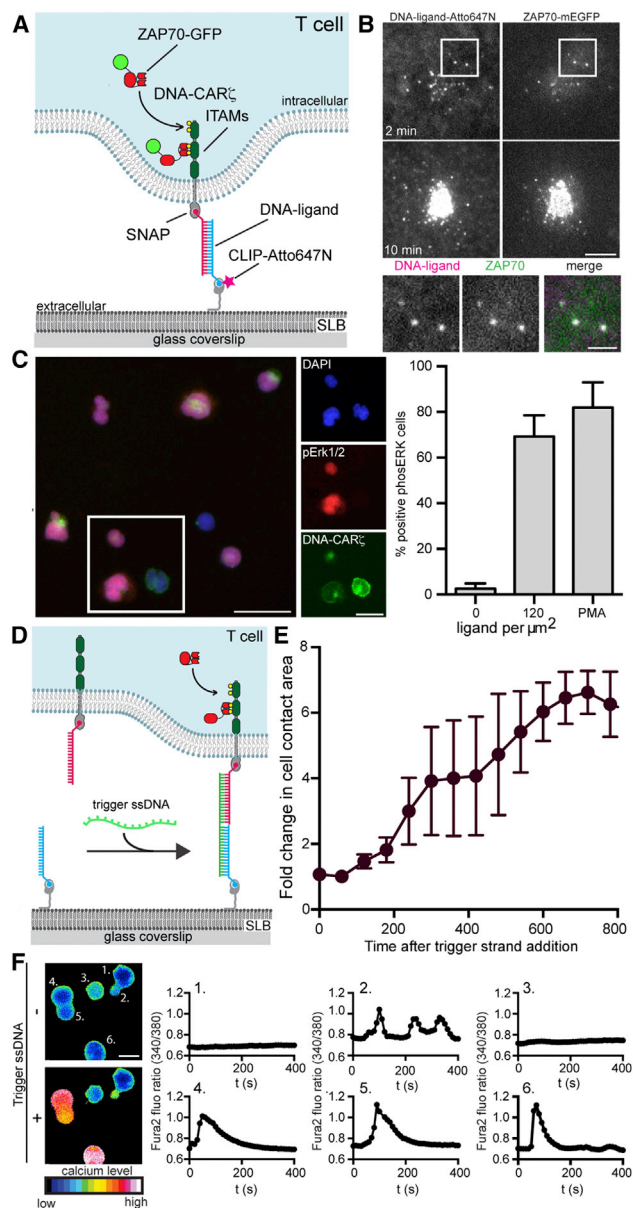
Figure 1. A DNA-CARζ Capable of Triggering T Cell Signaling

(A) Schematic of the DNA-based chimeric antigen receptor system (DNA-CARζ). The SNAPf tag and His10-CLIPf were covalently labeled with complementary strands of benzyl-guanine DNA and benzyl-cytosine DNA, respectively.

(B) TIRF microscopy images of a JRT3 Jurkat cell expressing ZAP70-GFP and DNA-CARζ labeled with 16-mer ssDNA after landing on a SLB with a complementary 16-mer strand (120 molecules per μm²). Microclusters of ligand-receptor complexes formed, recruited ZAP70-GFP (inset), and then moved centripetally and coalesced near the cell center. Scale bar, 5 μm; inset scale bar, 2 μm.

(C) To measure activation of the MAP kinase pathway, cells (15 min after SLB contact) were stained for phosphoERK (red); DAPI staining of nuclei (blue); and the DNA-CARζ (green). Bar, 50 μm. Insert shows higher magnification; bar, 20 μm. Quantification (see Figure S2; STAR Methods) of the MAP kinase pathway activation by the 16-mer DNA ligand compared to PMA (10 ng/ml) is shown. Mean ± SD of 6 experiments (>2,500 cells scored per experiment).

(D) A schematic of a triggerable DNA-CARζ.

(Chakraborty and Weiss, 2014; van der Merwe and Dushek, 2011). However, compelling evidence for kinetic proofreading is lacking, and it also remains controversial whether kinetic proofreading begins at the level of the receptor (Altan-Bonnet and Germain, 2005) or farther downstream (O'Donoghue et al., 2013).

Taking a reductionist approach to understand T cell signaling and ligand discrimination, we sought to engineer a T cell signaling system in which receptor-ligand affinity can be precisely tuned over a wide dynamic range without influence from other co-receptors (e.g., CD2, CD28; Wallace et al., 1993) or adhesion receptors (Mor et al., 2007). Previous work has shown that the extracellular ligand-binding regions of the TCR could be replaced with a single-chain antibody, which upon binding to its antigen on another cell membrane will initiate T cell signaling and activation (Eshhar et al., 1993; Gross et al., 1989; Irving and Weiss, 1991). Currently, T cells expressing such chimeric antigen receptors (CARs) are being tested for their ability to eliminate cancer cells (Sadelain et al., 2013). Based upon the work of CARs, we reasoned that the extracellular domains of the TCR and pMHC could be replaced by complementary strands of DNA and that DNA hybridization might act as the receptor-ligand interaction. The advantage of using DNA is that its nucleotide composition can be varied to provide exquisite and predictable control of the strength of the ligand-receptor interaction. Using this system and single-molecule live-cell imaging, we have found that a time-dependent conversation of a single ligated receptor into a cluster of ligated receptors is required for efficient TCR phosphorylation and the recruitment of ZAP70. The formation of receptor clusters arises from a dramatic increase in the ligand binding on-rate adjacent to pre-existing ligated receptors. These results, in combination with mathematical modeling, reveal that the spatial organization of receptor-ligand complexes provides an early proofreading step in T cell signaling.

RESULTS

Development and Characterization of a DNA-CAR

We created a nucleic acid-based synthetic DNA-CARζ that consists of a single-stranded DNA (ssDNA) covalently reacted to an extracellular SNAP tag protein that was fused to a transmembrane domain and intracellular CD3ζ chain (Figure 1A). To avoid any potential signaling cross-talk with the native receptor, we expressed this DNA-CARζ in a TCR-negative Jurkat cell line (JRT3) (Ohashi et al., 1985). To stimulate the DNA-CARζ, we replaced the antigen-presenting cell (APC) with a planar supported lipid bilayer (SLB) (Grakoui et al., 1999; Varma et al., 2006) functionalized with a freely diffusing CLIP protein covalently bound with a complimentary strand of ssDNA

(E) Cell spreading on the SLB as a function of time after adding the DNA trigger strand. The average fold-change after addition of trigger strand reflects the mean ± SEM from three separate experiments (3–7 cells per experiment).

(F) Pseudo-color image of calcium levels. The 340 nm/380 nm fura-2 emission ratio shows the change in intracellular calcium levels from the six cells after adding the DNA trigger strand. Bar, 10 μm.

See also Figure S1.

(STAR Methods). A single fluorescent dye also could be incorporated into the ligand DNA-CLIP complex in a non-perturbing and stoichiometric manner, allowing single-molecule observations. T cells and APCs initially interact through adhesion molecules (e.g., ICAM-LFA1) or other co-receptors, which also have signaling functions (Mor et al., 2007). To enable our DNA-CARζ T cells to adhere to the SLB without any co-stimulus, we made use of a synthetic DNA "adhesion system" that de-couples adhesion from cell signaling (Selden et al., 2012) (Figure S1A).

A high-affinity pMHC-TCR leads to increased intracellular calcium, MAP kinase activation, re-organization of the actin cytoskeleton, and the re-localization of transcription factors to the nucleus (Brownlie and Zamoyska, 2013). To assess whether the DNA-based CAR is capable of transmitting similar intracellular signals upon ligand binding, we first tested a high-affinity 16-mer DNA base-pair interaction (predicted off-rate of >7 hr, as estimated from computational analysis; Zadeh et al., 2011). The linear dimension of this 16-mer DNA-CARζ (∼13.4 nm, 4 nm each for the SNAP and CLIP tag enzymes [Daniels et al., 2000] and 5.4 nm for the 16-mer double-stranded DNA [dsDNA]) is similar to the 13 nm dimension of TCR-pMHC (Birnbaum et al., 2014; Choudhuri et al., 2005). When these cells were plated on SLBs with a high ligand density of ∼120 molecules per μm², we observed the rapid reorganization of ligand-bound receptors into submicron clusters that recruited the tyrosine kinase ZAP70-GFP (Figure 1B; Movie S1). These clusters were dynamic and translocated centripetally from the periphery to the cell center (Movie S1). This receptor behavior is similar to that reported for antibody- or pMHC-activated TCR (Grakoui et al., 1999; Kaizuka et al., 2007; Varma et al., 2006). The majority (∼65%) of the DNA-CARζ T cells also signaled through the MAP kinase cascade, as indicated by strong phosphoERK (pERK) staining of the nucleus (Figure 1C); this response was comparable to that produced by the strong stimulus of phorbol myristate acetate (PMA) (Figure 1C) and to that reported for TCR-pMHC in native T cells (Stefanová et al., 2003).

To examine the kinetics of signaling, we designed a system in which cells could be triggered to signal in a synchronous manner after they were adhered to the SLB through the inert DNA-adhesion system. To achieve such temporal control, we designed non-complementary ssDNA for the ligand and receptor and then introduced an oligonucleotide that could hybridize to both receptor and ligand DNA and thus bridge the two together (Figure 1D). Following the addition of this "trigger strand," the adhered cells spread rapidly (2–5 min), a result of the activation of actin polymerization (Figures 1E and S1B). Intracellular calcium also rose after ∼1 min (Figure 1F; Movie S2), and CD69, a TCR activation marker, was expressed on the cell surface at 4 hr (Figure S1D). The timing of these responses are similar to those reported previously (Irving and Weiss, 1991). Thus, the DNA-based CARζ induces similar intracellular signaling responses to those described for T cells triggered through TCR and pMHC.

## Ligand Discrimination by the DNA-CARζ

Next, we used automated microscopy and image analysis of pERK staining as a readout to test how signaling is influenced

by the length and sequence of the DNA (Figures S2A and S2B). For these experiments, we used the direct hybridizing ligand-receptor pair (Figure 1A), given that the ligand concentrations on the SLB can be carefully controlled and varied (STAR Methods). For length, we decreased the number of hybridizing bases from 16 to 13, 12, or 11 and added poly-dT to the ligand to maintain the overall oligo length (see STAR Methods for discussion of how a change from dsDNA to ssDNA might affect overall receptor-ligand dimensions). Compared to the 16-mer oligo, ligand dose-response curves of the 13-mer and 12-mer oligo ligands produced progressively weaker MAP kinase signaling (Figures 2A and 2B). The 11-mer did not elicit a measurable pERK response above background, even at the highest ligand density. We then attempted to restore signaling to the 11-mer by mutating adenine/thymine (A/T) base pairs to guanine/cytosine (G/C) base pairs, which increases the binding free energy of hybridization (Table S1). Remarkably, a single A/T-to-G/C mutation converted the initial non-signaling 11-mer receptor to one that could elicit a pERK response at high ligand densities, and each additional G/C mutation increased the potency of the DNA receptor (Figure 2C).

Because theoretical models and biochemical data have suggested that the bound time of the TCR and pMHC plays a critical role in signaling (Chakraborty and Weiss, 2014; Davis et al., 1998; Malissen and Bongrand, 2015), we used single-molecule total internal reflection fluorescence (TIRF) microscopy to directly measure the lifetime of individual DNA receptor-ligand interactions at the cell-SLB interface (O'Donoghue et al., 2013) (Figures 2D and S2). The bound time of the ligand for the receptor displayed a roughly exponential distribution (Figures 2D, S2E, and S2F) with an observed half-life of ∼2 s for the non-activating 11-mer and a half-life of ∼19 s for the 11-mer with three additional G/C bases (Figure 2D). The much slower off-rate of the 16-mer DNA ligand (predicted to be hours) could not be determined accurately, as these measurements were limited by the rate of photobleaching (Figure S2E). Overall, the ligand bound times and the ligand densities on the SLB required for half-maximal responses are similar to those reported for TCR-pMHC in comparable bilayer activation experiments (O'Donoghue et al., 2013). Collectively, these results clearly show that increasing the GC base pairing of the receptor results in a longer ligand-receptor interaction and that the T cell signaling response can distinguish between DNA receptor-ligand interactions with small difference in binding free energy (∼1 kcal/mol, STAR Methods).

Single-Molecule Imaging of DNA-CARζ Phosphorylation

We next wanted to examine how the extracellular receptor-ligand bound time is translated into intracellular biochemistry, the first step being the phosphorylation of the ITAM domains of the DNA-CARζ receptor. Phosphorylation of the ITAMs leads to the recruitment of the kinase ZAP70, which phosphorylates downstream targets (Brownlie and Zamoyska, 2013). To measure phosphorylation of DNA-CARζ in live cells in real time, we examined the recruitment of ZAP70-GFP from the cytosol to receptor-ligand complexes by TIRF (Figures 3, S3E, S3F, and S4). We first used the 16-mer at a ligand density of 0.1 molecules per μm², a density below the threshold required to elicit a
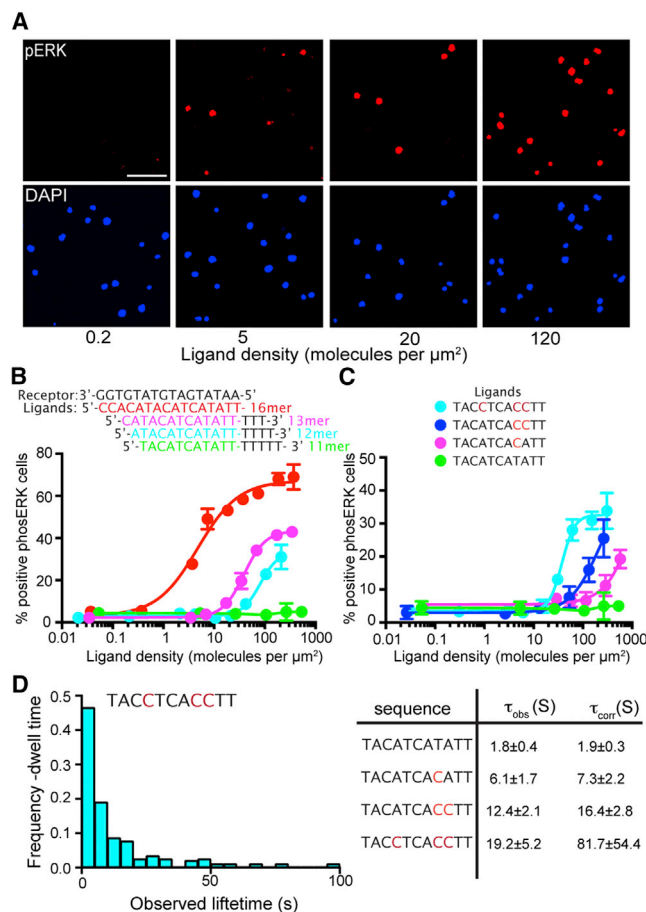
Figure 2. Modulation of T Cell Activation by DNA-CARζ Length and Sequence

(A) Thresholded images of phophoERK and DAPI staining of JRT3 cells responding to increasing 16-mer DNA ligand on SLBs (15 min). Scale bar, 100 μm. See also Figure S2.

(B) Dose-response curves for DNA ligands of varying hybridization lengths. The total ligand DNA length remained constant by adding non-hybridizing Ts. Mean ± SD (n = 3).

(C) Stepwise conversion of A/T to G/C base pairs increases the potency of the 11-mer DNA ligand for inducing phosphoERK signaling. Scale bar, 100 μm. Mean ± SD of each ligand density measured in triplicate from one representative experiment.

(D) Single ligand-receptor lifetimes by TIRF microscopy. An example distribution of lifetimes from one DNA ligand. The observed (τ_{obs}) and photobleach-corrected (τ_{corr}) lifetimes are shown for the 11-mers (mean ± SEM from three separate experiments); for data of 13-mer and 16-mer and all histograms, see Figure S2.

pERK response. Under these conditions, single receptor-ligand binding interactions can be observed clearly (Figures 3A and S4A; Movie S3). However, surprisingly only ∼6% of the ligand-binding events (trackable for 30 s or more) led to detectable ZAP70-GFP recruitment, despite the long bound time of the ligand-receptor interaction (Figure 3B). In these rare cases, ZAP70-GFP recruitment was transient and lasted less than ∼20 s (Figure 3C); this single-molecule measurement reflects the off-rate of ZAP70, as the 16-mer has an off-rate on the hour timescale. In this experiment, non-fluorescent endogenous

ZAP70 could potentially outcompete ZAP70-GFP for binding to the ligated receptor, thus affecting measurements and conclusions. Thus, we repeated these experiments in the P116 ZAP70-null Jurkat cell line (Williams et al., 1998); very similar results were observed (Figures S4B–S4D), confirming that ZAP70 is not efficiently recruited to single receptor-ligand complexes at low ligand densities. These results indicate that a long-lived ligand-binding interaction per se is not sufficient to trigger receptor phosphorylation.

Because binding of the high-affinity 16-mer ligand to a single receptor did not lead to stable receptor phosphorylation, we next wished to understand what additional events might be needed to initiate this first step in signaling. To answer this question, we performed single-molecule studies at a 10-fold higher 16-mer ligand density (16-mer ligand density of 1 molecule per μm²), a regime in which 20% of the cells generate a pERK response (Figure 3D) and the ligand density was still low enough to enable clear single-molecule imaging. At 1 molecule per μm², single 16-mer receptor-ligand pairs formed initially and then grew into small clusters on the membrane within a few minutes of cell contact with the SLB (Figures 3D and S4E; Movie S4). By quantitating the fluorescence increase of these small receptor-ligand clusters, we could estimate how many bound ligands were present in a cluster at the initial moment of ZAP70-GFP recruitment (Figures 3D and S3). This analysis revealed that ZAP70-GFP is recruited more efficiently to clusters containing three or more ligated receptors (∼80%) compared with single ligated receptors (∼20%) (Figure 3E). Furthermore, the bound time of ZAP70-GFP on a single ligated receptor was short (half-life of ∼10 s; Figure 3F and example 4 in Figure S4E), as reported at the lower ligand density on the bilayer (Figure 3C). In striking contrast, nearly half of ZAP70-GFP molecules (48%) remained associated for 100 s or more with small receptor clusters (Figure 3F). Thus, clusters composed of just a few bound receptors become phosphorylated and stably recruit ZAP70-GFP, whereas single ligated receptors only occasionally and transiently bind ZAP70-GFP.

We next investigated whether the dynamics of ZAP70-GFP recruitment to a DNA-CAR consisting of all TCR subunits (DNA-CAR$_{TCR}$) were different from those of DNA- CARζ, which contains just the CD3ζ chain. To generate the DNA-CAR$_{TCR}$, the extracellular SNAP-tag was fused to the N terminus of the TCR β subunit, which positions the SNAP-tag close to the plasma membrane in a comparable location to the DNA-CARζ. When expressed in the JRT3 cell line (which is null for the β subunit), the SNAP-β subunit assembles with the other TCR subunits (α chain and the ITAM-containing CD3ε, δ, γ, ζ chains), and the full TCR complex then is able to traffic from the ER to the cell surface (Figures 4A, S5A, and S5B) (Ohashi et al., 1985). At a low density of 0.1 per μm², the minority (∼21%) of single DNA-CAR$_{TCR}$ receptors bound with 16-mer ligand recruited ZAP70 (Figure 4B; Movie S5). As was observed with the DNA-CARζ, the ZAP70 dwell time at the single ligand-bound DNA-CAR$_{TCR}$ was transient (mean dwell time of ∼20 s) (Figures 4C, 4D, and S5C). At this low ligand density, we also observed the rare formation of a small cluster consisting of two 16-mer ligands (∼5% of total events; Figure 4B). Of these rare events (n = 8), ∼63% recruited ZAP70 (Figure 4B; see example 3 in Figure S5C), a result
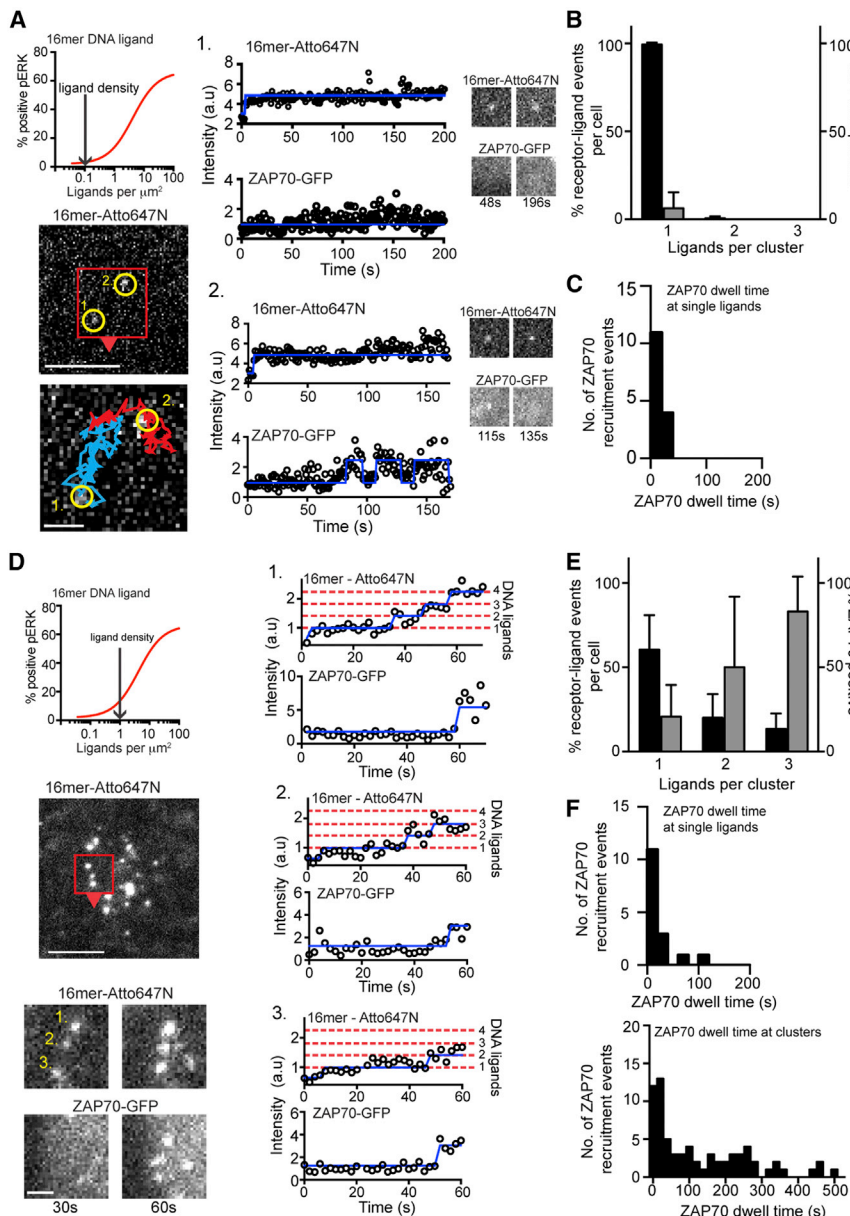
Figure 3. Receptor Clustering Increases the Probability of ZAP70 Recruitment

Ligand and ZAP70-GFP binding to DNA-CARζ by TIRF imaging with a 16-mer ligand at 0.1 (A–C) and 1 ligand per μm² (D and E). Dose-response curves (A and D) are based on data in Figure 2B. The blue line overlaid on the fluorescence intensity represents detected step changes marking new ligand binding or ZAP70 recruitment events. The dashed red lines mark the quantal ligand fluorescence intensities determined using a hidden Markov model analysis (see Figure S3 and STAR Methods). Single or multiple ligand-binding events that could be followed for >30 s were scored for ZAP70-GFP recruitment. The initial ZAP70-GFP recruitment was referenced to the number of bound ligands (as in A and D).

(A) TIRF images of Atto647N-labeled 16-mer DNA ligands. Left panel, single bound ligands are marked by yellow circles. Bar, 5 μm. Region of interest overlaid with tracked single-molecule trajectories. ROI bar, 1 μm. Right panels, fluorescence-intensity time series for the 16-mer ligand and the corresponding ZAP70-GFP fluorescence intensity. Ligand 1, example of a ligand-receptor pair that does not recruit a ZAP70-GFP. Ligand 2, a less common example of ZAP70-GFP recruitment (often transient as shown here) to a single bound 16-mer ligand.

(B) Quantification of ZAP70-GFP recruitment at 0.1 ligands/μm² of 16-mer. Bar plot shows the percentage of single ligated receptors and clusters (black bars) and percentage of ZAP70 recruitment (gray bars) for single bound ligands that can be tracked for >30 s. Mean ± SD from n = 9 cells.

(C) Quantification of ZAP70 dwell times at single bound 16-mer ligands (n = 15).

(D) TIRF images of 16-mer DNA ligands at 1 ligands/μm². Bar, 5 μm. Region of interest (red box) shows three ligand-receptor clusters (labeled 1–3). ROI bar, 1 μm. Fluorescence-intensity time series from the DNA ligand and ZAP70-GFP of the three microclusters shown on the right. For additional traces, see Figure S4 and Movies S3, S4, S5, and S6.

(E) Quantification of ZAP70 recruitment at 1 ligands/μm² of 16-mer. Organization of bar plot same as shown in (B). Results are mean ± SD from n = 6 cells.

(F) Distribution of ZAP70 dwell times at single bound receptors (n = 16) and receptor-ligand clusters (n = 70). For 32 clusters with ZAP70 dwells time of > 100 s, the measurement was truncated by the end of image acquisition.

See also Figure S4.

that is consistent with a mechanism of small clusters of receptors being more readily phosphorylated than single ligated receptors. When the 16-mer ligand density was raised to 1 molecule per μm², clusters of ligand-bound DNA-CAR_TCR began to form more readily, and these clusters more efficiently recruited ZAP70 (90%) compared with single ligated receptors (20%) (Figure 4E; examples in Figure S5D). Furthermore, the ZAP70 dwell time at single ligand-receptor complexes (~20 s; Figure 4F) was much shorter compared with clusters; one-third of receptor clusters displayed ZAP70-GFP association times of >100 s (Figure 4F). These results reveal similar behaviors of DNA-CAR_TCR and DNA-CARζ; in both instances, small receptor-ligand clusters

more efficiently and stably recruit ZAP70 compared to single ligated receptors.

Comparison of Low- and High-Affinity Ligands

We next sought to compare the behaviors of a low-affinity (13-mer DNA strand) and high-affinity receptor (16-mer) interacting with their cognate ligands at the same density on a supported lipid bilayer (1 molecule per μm²). At this ligand density, at which only the higher affinity 16-mer elicits a pERK response (Figure 2B), the two receptors showed considerable differences in their abilities to form clusters. In the case of the 16-mer, many (5–20) receptor clusters formed a few minutes after cells landed
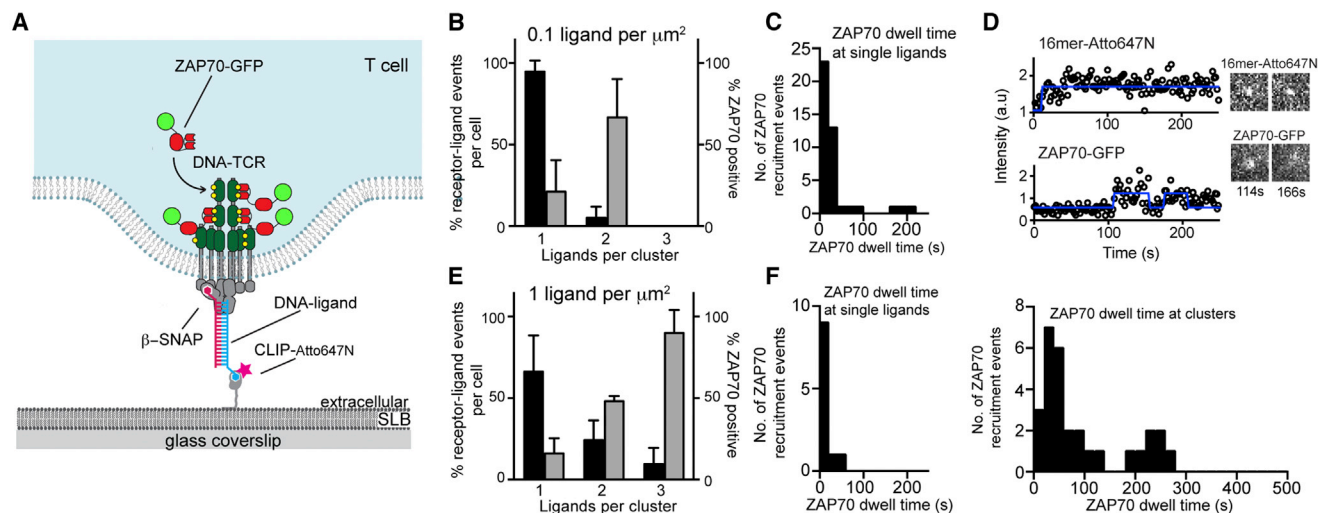
Figure 4. Receptor Clusters Increase the Probability of ZAP70 Recruitment to a DNA-Based CAR System Consisting of the Complete TCR

(A) Schematic of a DNA-based CAR consisting of the complete TCR (DNA-CAR$_{TCR}$).

(B) Quantification of ZAP70-GFP recruitment to DNA-CAR$_{TCR}$ at 0.1 ligands/μm^2 (16-mer). Bar plot shows the percentage of single bound ligand receptors and clusters (black bars) and percentage of ZAP70 recruitment (gray bars). Mean ± SD from n = 8 cells.

(C) Quantification of ZAP70 dwell time at single bound 16-mer ligands (n = 42).

(D) A typical example of a transient recruitment of ZAP70-GFP to a single DNA-CAR$_{TCR}$. See also Figure S5C.

(E) Quantification of ZAP70-GFP recruitment to DNA-CAR$_{TCR}$ at 1 ligands/μm^2 (16-mer). Organization of bar plot same as shown (B). Mean ± SD from n = 3 cells.

(F) Distribution of ZAP70 dwell times at single bound receptors (n = 11) and receptor clusters (n = 30).

See also Figure S5.

on the bilayer (Figure 5A), and many of these clusters were long lived (44% persisting for >100 s; Figure 5B). During the same period of time with the 13-mer ligand, single ligand-receptor binding events were observed but cluster formation was very rare (Figure 5A). A few small clusters of ligated 13-mer receptors began to appear on the cell surface after 15 min (Figure 5A; Movie S6), but most of these clusters disassembled rapidly (mean half-life of ∼21 s; Figure 5C). As described earlier for the 16-mer ligand, ZAP70-GFP recruitment was observed with ∼50% for clusters of three or more 13-mer ligands and infrequently (∼2%) observed with single 13-mer ligand-receptor complexes (Figures S6A and S6B). Because these 13-mer receptors clusters were transient, correspondingly, ZAP70-GFP also dissociated from the membrane (Figure S6C). At 30-fold-higher 13-mer density on the bilayer (30 molecules per μm^2; where 20% of the cells become pERK positive; Figure 2B), DNA-CARζ clusters now formed within a few minutes of the cell landing on the bilayer (Figure 5A). These clusters had a similar stability to that seen with the 16-mer at 1 molecule per μm^2 (36% persisting for >100 s; Figure 5B) and efficiently recruited ZAP70-GFP (Figure S6C). In summary, the strong and weak ligands formed clusters and stably recruited ZAP70 at different ligand densities; the ligand density required for ZAP70 recruitment also correlated with that required to generate a rapid downstream pERK signaling response (Figure 2B).

Enhanced On-Rate of Ligand Binding Adjacent to Pre-existing Ligand-Receptor Complexes

We anticipated that receptor-ligand clusters might form through collisions between diffusing ligated receptors. However, such

events were rarely observed. More commonly, a single DNA-CARζ (Figure 6A; Movies S4 and S7) or DNA-CAR$_{TCR}$ (Figure S6D) grew in fluorescence intensity in roughly quantized steps. This result is best explained by new ligand-binding events occurring near to pre-existing receptor-ligand complexes. We quantified the rate of new DNA-CARζ ligand-binding events occurring adjacent to a pre-existing receptor ligand (using an area of a diffraction-limited spot) versus the rest of the plasma membrane (area of the total cell footprint on the SLB observed in the TIRF field). This analysis revealed that the area-normalized on-rate is at least 350-fold higher near a pre-existing ligated receptor or small receptor cluster compared to the rest of the membrane (Figure 6B). We observed a similar phenomenon of an enhanced ligand-binding rate at pre-existing bound DNA-CARζ-ligand complexes in cells treated with latrunculin to depolymerize actin, although the magnitude of the effect was diminished (75-fold enhancement; Figures S6E and S6F). After small clusters formed, we observed that they diffused and could sometimes fuse with one another to form larger-sized clusters (Figure 6A; Movie S7). In summary, enhanced ligand on-rate adjacent to pre-existing ligated receptors dominates the formation and growth of receptor clusters. Potential mechanisms that could explain this result are presented in the Discussion.

DISCUSSION

In summary, our data, for both a CAR and a complete TCR, show that the binding energy of extracellular DNA hybridization can be transduced across the plasma membrane to trigger intracellular receptor phosphorylation and further downstream signaling. We
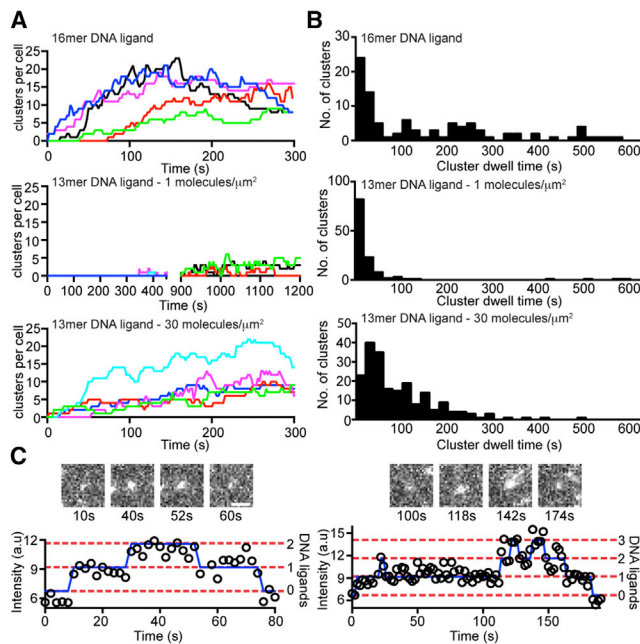
Figure 5. Difference in Microcluster Formation by Low- and High-Affinity Ligands with DNA-CARζ

(A) Formation over time of ligand-receptor clusters (defined as a diffraction limit structure containing ≥ 2 ligands) for individual cells (colors) at 1 ligands/μm^2 for the 16-mer and 30 ligands/μm^2 for the 13-mer. t = 0 is defined as the point of image acquisition, generally within 1–2 min of adding cells to the SLB.

(B) Distribution of dwell times for ligand-receptor clusters composed of 16-mer (n = 94 from 6 cells; 35 clusters with >100 s dwell times were truncated by the end of image acquisition) and 13-mer ligands (n = 125 from 6 cells; 6 clusters similarly truncated by image acquisition) at 1 ligands/μm^2 and 13-mer DNA ligand at 30 ligands/μm^2 (n = 203 from 5 cells; 26 clusters truncated by image acquisition).

(C) TIRF images and intensity time series showing the formation of transient receptor-ligand clusters of 13-mer DNA ligand at 1 ligands/μm^2. The fluorescence time series were analyzed as described in Figures 3 and S3.

See also Figure S6.

show that a longer bound-time between a ligand and its receptor and higher ligand densities synergize to promote receptor clustering and that the formation of long-lived receptor clusters substantially increases the probability of receptor phosphorylation and ZAP70-GFP recruitment compared with even long-lived single ligated receptors. These results provide new insights into the mechanism of TCR signaling and the basis of ligand discrimination, as discussed below.

The Role of Receptor Clustering in TCR Signaling

Using DNA hybridization, we could examine a ligand (16-mer) with a much longer predicted off-rate (> 7 hr) than the strongest agonist pMHCs (~1 min; Gascoigne et al., 2001; O'Donoghue et al., 2013). Surprisingly, despite the long engagement of the 16-mer, the majority of single 16-mer ligand-receptor pairs did not become phosphorylated and recruit ZAP70. In instances where ZAP70 was recruited, its residence time was short (~10–20 s), which is similar to the off-rate measured for ZAP70 from CD3ζ (Klammt et al., 2015). Thus, we suspect that these
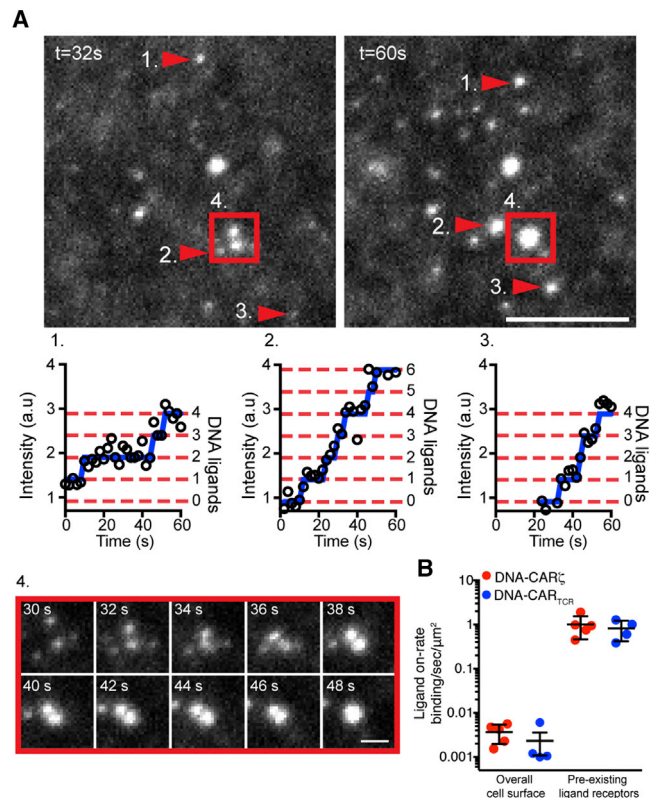
**Figure 6. Formation of Microclusters from Single Ligand-Receptor-Binding Event**

(A) A TIRF image of receptor-bound 16-mer DNA ligand; receptor-ligand clusters grow by adjacent ligand-binding events (red arrows numbered 1–3) and by merging and fusion (red box numbered 4). Bar, 2.5 μm. See Movie S7. Clusters grow by sequential addition of newly bound ligand; the blue lines overlaid on the fluorescence intensities are detected step changes (see STAR Methods; Figure S3). Time series (red box, numbered 4) below follows fusion of two clusters (Bar, 1 μm).

(B) The rate of new ligand-binding events near to an existing receptor-bound ligand (quantal intensity increase in an existing diffraction-limited spot) or outside of these zones (sudden appearance of a new bound ligand in the contact area between the cell and SLB) for DNA-CARζ (red) and DNA-CAR$_{TCR}$ (blue). The ligand-receptor on-rate is expressed as events per second per μm^2 membrane surface area (using 0.126 μm^2 for a diffraction-limited spot). Mean ± SEM from n = 125 binding events from 5 cells and n = 60 binding events from 4 cells for the DNA-CARζ and DNA-CAR$_{TCR}$, respectively.

See also Figure S6D.

transient recruitment events reflect a relatively rare dual-phosphorylation event of an ITAM on CD3ζ by Lck and the recruitment of ZAP70, followed by the dissociation of ZAP70 and the rapid dephosphorylation of CD3ζ by CD45 to prevent rebinding of ZAP70. Some models of TCR signaling propose that receptor-ligand dwell time is the primary determinant of T cell receptor activation (Chakraborty and Weiss, 2014; Malissen and Bongrand, 2015). However, our results indicate that a long receptor-ligand engagement per se is insufficient to induce effective downstream signaling through ZAP70 recruitment to the plasma membrane.

Our results provide strong support for the role of clusters in T cell signaling and are consistent with statistical analysis
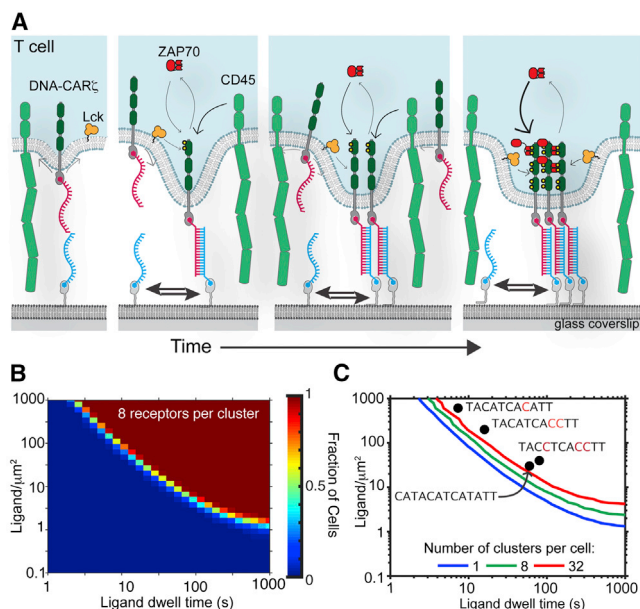
Figure 7. A Signaling Model for T Cell Ligand Discrimination based on Receptor Clustering and ZAP70 Recruitment

(A) Model of for receptor clustering and phosphorylation. A single receptor-ligand interaction pins the two membranes in close apposition; unbound ligands that diffuse into this region are in closer proximity to and can more readily bind a receptor. Clustered receptors more effectively exclude the phosphatase CD45 and become phosphorylated; for lower-affinity ligands, receptor clusters and phosphorylation can be reversed by ligand dissociation, providing a mechanism for kinetic proofreading (see Discussion).

(B and C) A theoretical signaling model, incorporating experimentally measured parameters (Figure S7) was used to perform stochastic simulations of cells interacting with a ligand-functionalized SLB. Simulations were performed at ligand densities between 0.01 and 1,000 molecules/μm² and ligand dwell times (1–1000 s) for a fixed time interval of 500 s and repeated for 250 cells at each point in this parameter space. The simulation output was timeseries data of ligand binding, cluster formation, and ZAP70 recruitment, and heatmaps were generated showing the fraction of cells showing a defined characteristic of ZAP70-positive receptor-ligand clusters (see B and Figure S7K).

(B) Fraction of simulated cells with at least one receptor-ligand cluster containing eight ZAP70-positive receptors.

(C) Increasing ligand density and affinity results in an increasing number of ligand-receptor clusters. The 20% contour of these heatmaps was analyzed to demarcate regions within this parameter space where the simulation showed >20% of simulated cells forming the indicated number of clusters with a minimum of eight ZAP70-positive receptors. On this plot, the experimental data are shown for the ligand densities and dwell times at which the indicated DNA ligands elicited 20% phosphoErk-positive cells (Figures 2 and S2).

indicating that the small clusters of ligated pMHC-TCR activate downstream calcium signaling (Manz et al., 2011). In contrast to the single ligated receptors, small clusters of three ligated receptors are ~90% occupied with ZAP70, and the dwell time of the ZAP70 at the membrane increases substantially. We have observed hundreds of instances of a time-dependent conversion of single ligated receptors into clusters, which then became active in recruiting ZAP70. Interestingly, the dwell of ZAP70 at these small receptor clusters does not follow a simple exponential, and a subset of the clusters stably recruit ZAP70

for >2 min (Figure 3F). Possible mechanistic explanations for such enhancement in ZAP70 dwell time could be due to dissociation and rapid rebinding to ITAM motifs as a result of high local concentrations in receptor-ligand clusters. Alternatively, clustering might enhance the phosphorylation of ZAP70 at activating tyrosine residues by Lck or other ZAP70 molecules, a modification that has been shown to enhance ZAP70 affinity for the phosphorylated ITAMs in vitro (Klammt et al., 2015).

As described in the "kinetic segregation" model (Davis and van der Merwe, 2006), regions of membrane bending created by receptor-ligand interactions exclude the large transmembrane domain of CD45 and thus shift an equilibrium reaction between the receptor kinase (Lck) and the phosphatase (CD45) to favor net receptor phosphorylation. We speculate that receptor clusters become more stably phosphorylated than single ligated receptors because they more effectively exclude the transmembrane phosphatase CD45 (Figure 7A). Exclusion of the transmembrane phosphatase CD45 has been observed for receptor clusters composed of many tens or hundreds of molecules (James and Vale, 2012; Varma et al., 2006). However, if CD45 exclusion underlies the receptor phosphorylation observed in this study, then these results suggest that single ligated receptors are ineffective at preventing CD45 from acting upon phosphorylated TCR, but that clusters even as small as 2–4 receptors can create physical zones that limit access of CD45 phosphatase to phosphorylated ITAMs (Figure 7A). The expected diameters of the exclusion zones created by these small receptor clusters are well below the diffraction limit of light and most super-resolution light microscopy techniques but could be examined by electron microscopy in future studies.

The manner in which receptor clusters form was also surprising. Our prior model speculated that single receptor ligands rapidly diffuse in the plane of the membrane and coalesce into clusters (James and Vale, 2012). Instead, this work shows that clusters form predominantly through an enhancement of the ligand on-rate adjacent to a pre-existing ligated receptor(s). The mechanism behind the dramatic acceleration of the ligand on-rate near to pre-existing ligand receptors is not established. This observation might arise from heterogeneities in the concentration of the TCR within the membrane, potentially through mechanisms of receptor nano-scale clustering (Reth, 2001) or dynamic changes in local receptor concentration induced by ligand binding (Dushek and van der Merwe, 2014). EM and super-resolution microscopy studies also have suggested that the TCR is organized into small nano-clusters consisting of anywhere between 5 and 30 receptors (Lillemeier and Davis, 2011; Schamel et al., 2005). However, the nano-scale organization of the unbound TCRs remains controversial with conflicting data (James et al., 2007), and the mechanism for how nano-clusters of unligated TCR or DNA-CARs might assemble and be held together is unknown. Furthermore, we observed enhanced ligand binding with both DNA-CARζ and DNA-CAR_{TCR}, which would suggest that, if nano-scale organization exists and is responsible for the enhanced on-rate, it can not be specific to the native TCR.

An alternative explanation for a spatial enhancement in ligand binding evokes the closer physical proximity of the two membranes established by an initial receptor-ligand interaction

(Choudhuri et al., 2005; James and Vale, 2012) (Figure 7A). Theoretical studies have suggested that unbound receptors and ligands on opposite membranes that diffuse into zones of close contact interact more readily, as compared to regions where the two membranes are further apart (Hu et al., 2013; Qi et al., 2001). Computational simulations also have shown that a close membrane contact zone created by an initial receptor-ligand bond facilitates subsequent binding events, resulting in a net cooperative binding effect (Krobath et al., 2009). Our experimental results are consistent with the results of this computational study.

Spatial Organization as a Mechanism of Ligand Discrimination

Like prior studies with different pMHC ligands interacting with TCR (Gascoigne et al., 2001; Grakoui et al., 1999; Huppa et al., 2010), we show in this study that T cells can discriminate between DNA ligands with relatively small differences (a few fold) in receptor-bound times (Figure 2). The molecular basis by which T cells convert such small energy differences in receptor-ligand binding into all-or-none signaling responses and cell activation remains an important unsolved problem. A general model for this type of ligand discrimination, called "kinetic proofreading" (McKeithan, 1995), proposes that a signaling competent state requires a series of reactions that require the continuous receptor occupancy; if the ligand dissociates, then these reactions are rapidly reversed, terminating signaling and resetting the receptor to its initial inactive state. Although this theory is appealing, the series of reversible reactions that lead to a "signaling-competent state" are unknown, although many diverse models have been proposed, including receptor conformational changes, dimerization, and phosphorylation reactions (Chakraborty and Weiss, 2014; Malissen and Bongrand, 2015; van der Merwe and Dushek, 2011).

Our results suggest that the spatial organization of receptors provides a mechanism for kinetic proofreading in ligand discrimination. In line with the kinetic proofreading model, the initial ligand-receptor complex has low signaling output and must undergo a series of time-dependent and reversible steps to form a signaling-competent receptor cluster. Weaker ligands, as seen with the 13-mer at 1 molecule per μm^2 (Figure 5), dissociate faster than new binding events occur, prohibiting the build-up of stable signaling-competent receptor clusters.

To quantitatively assess whether the time-dependent formation of receptor clusters provides a mechanism for ligand discrimination, we constructed a kinetic proofreading mathematical model that incorporates our experimentally determined on- and off-rates of receptor-ligand binding and ZAP70 interaction with the membrane (Figure S7). Using our experimentally derived rate constants, we computed the statistics of the number of ligated receptors in a cluster at the moment of ZAP70 recruitment, the propensity of single receptors or receptor clusters to become ZAP70 positive, and the distribution of cluster lifetimes (Figures S7G–S7I). The results of our simulations of the above parameters agreed well with experimental data, thus validating the overall model (Figure S7).

To understand how the formation of ZAP70-positive clusters could provide thresholds for a discriminatory signaling output,

we conducted stochastic simulations of the model in a parameter space of ligand density and affinity. We analyzed the results of the simulation by plotting the fraction of simulated cells that formed clusters consisting of a few ZAP70-positive receptors (here chosen to be 8; variations of the threshold in Figure S7J) (Figure 7B). The simulations revealed a sharp transition ($\sim$3-fold changes in ligand density or ligand affinity) between a regime of a low probability of cluster formation (<20% of cells; blue area in Figure 7B) to a regime of high-probability receptor clustering with stable ZAP70 recruitment (>80% of cells) (red/brown area in Figures 7B and S7). We also analyzed simulations that incorporated the very long ZAP70 dwell times as shown in Figures 3 and 4. These simulations also revealed similar sharp transitions (Figures S7K and S7L) but revealed an even greater probability of stable ZAP70 association at clusters of high-affinity ligands at low ligand densities, thus further enhancing ligand discrimination of this kinetic proofreading model. In summary, our simulations reveal a switch-like response for receptor cluster formation. This behavior can amplify small differences in ligand affinity or density into dramatically different outputs of ZAP70 recruitment.

We next analyzed how well our model correlated with the experimentally observed downstream signaling outputs of phosphoErk (evaluated as 20% pERK activation threshold; Figure 2B). We found that pERK signaling threshold lay inside the region of parameter space in which the signaling model generated multiple clusters that stably recruited ZAP70 (Figures 7C and S7J). In the regime for which we measured pERK signaling, the slope of the data and the activation threshold of the model were similar, which reflects a similar degree of ligand discrimination. The model predicts that the weaker 11-mer DNA ligand (TACATCATATT), with an $\sim$2 s dwell time (Figures 2B and 2D), would generate clusters with stable ZAP70 at a density of $\sim$900–1000 ligand per μm^2 (Figures S7K–S7L) and thus would trigger a pERK response. However, our experimental analysis revealed no discernible signaling for the 11-mer ligand (Figure 2), implying that the degree of ligand discrimination in our mathematical model is lower than that observed experimentally. Thus, kinetic proofreading through receptor clustering provides a partial but not complete explanation for ligand discrimination and implies that other kinetic proofreading steps may lie downstream of ZAP70 recruitment to receptor clusters.

Sensitivity of T Cell Signaling

The bound time of the 13-mer DNA receptor ligand ($\sim$24 s) is comparable to that of TCR-pMHC complexes that have been extensively studied (few tens of seconds; Gascoigne et al., 2001). This DNA ligand also elicited T cell signaling at comparable densities (10–100 molecules per μm^2) to those used to stimulate native T cells with pMHC on supported lipid bilayers (Grakoui et al., 1999; Manz et al., 2011). However, in the more physiological context of the APC-T cell conjugate, T cells respond to lower levels of pMHC (Altan-Bonnet and Germain, 2005; Huang et al., 2013). In these contexts, T cell signaling is likely facilitated by other factors, such as force-induced mechanical changes in the TCR (Liu et al., 2014), adhesion molecules that also form signaling complexes (e.g., LFA-1-ICAM1)

(Springer, 1990), low-affinity ligands (e.g., self pMHC) (Stefanová et al., 2002; Wülfing et al., 2002), and numerous other co-receptors that enhance signaling (e.g., CD4/8, CD28-B7, CD2-CD58) (Chen and Flies, 2013). In future work, these additional components can be added to the DNA-CARζ system to determine whether they enhance the sensitivity of signaling and, if so, understand how they affect the assembly and phosphorylation kinetics of receptor clusters as well as influence downstream biochemical events that lead to T cell activation.

STAR★METHODS

Detailed methods are provided in the online version of this paper and include the following:

- KEY RESOURCES TABLE
- CONTACT FOR REAGENT AND RESOURCE SHARING
- EXPERIMENTAL MODEL AND SUBJECT DETAILS
  - Cell Culture
- METHOD DETAILS
  - Generation of DNA-CARs and ZAP70 Constructs
  - DNA-CARζ-GFP
  - DNA-CARζ-IRESpuro
  - DNA-CAR$_{TCR}$-IRESpuro
  - pHR-TCRα-E2A-SNAPf:TCRβ-P2A-CD3ε-P2A-CD3ζ
  - ZAP-GFP
  - Lentiviral Production and Generation of Stable Expressing JRT3 Cell Lines
  - Imaging Chambers and Supported Lipid Bilayers
  - Protein Expression, Purification, and Labeling
  - Synthesis of Benzylguanine-Conjugated DNA Oligonucleotides
  - DNA Ligand and Receptor Sequence Design
  - DNA-Based Adhesion System
  - BG-DNA Labeling of JRT3 Cells Expressing DNA-CAR
  - CD69 Expression
  - Calcium Imaging and Analysis
  - PhosphoERK Data Acquisition and Analysis
  - Imaging Single Ligand-Receptor Dwell Time
  - Imaging and Analysis of Single Ligand-Receptor Interactions and ZAP70 Recruitment
  - Construction of a Stochastic Signaling Model
  - Ligand Discrimination in the Model
  - Stochastic Simulation Method
- QUANTIFICATION AND STATISTICAL ANALYSIS
  - PhosphoERK Quantification and Analysis
  - Quantification and Analysis of Single Ligand-Receptor Dwell Time
  - Hidden Markov Model Analysis of Receptor-Ligand Cluster Assembly and ZAP70 Recruitment
- DATA AND SOFTWARE AVAILABILITY
- ADDITIONAL RESOURCES

SUPPLEMENTAL INFORMATION

Supplemental Information includes seven figures, one table, and seven movies and can be found with this article online at http://dx.doi.org/10.1016/j.cell.2017.03.006.

REFERENCES

Altan-Bonnet, G., and Germain, R.N. (2005). Modeling T cell antigen discrimination based on feedback control of digital ERK responses. PLoS Biol. 3, e356.

Birnbaum, M.E., Mendoza, J.L., Sethi, D.K., Dong, S., Glanville, J., Dobbins, J., Ozkan, E., Davis, M.M., Wucherpfennig, K.W., and Garcia, K.C. (2014). Deconstructing the peptide-MHC specificity of T cell recognition. Cell 157, 1073–1087.

Bronson, J.E., Fei, J., Hofman, J.M., Gonzalez, R.L., Jr., and Wiggins, C.H. (2009). Learning rates and states from biophysical time series: a Bayesian approach to model selection and single-molecule FRET data. Biophys. J. 97, 3196–3205.

Brownlie, R.J., and Zamoyska, R. (2013). T cell receptor signalling networks: branched, diversified and bounded. Nat. Rev. Immunol. 13, 257–269.

Chakraborty, A.K., and Weiss, A. (2014). Insights into the initiation of TCR signaling. Nat. Immunol. 15, 798–807.

Chan, Y.-H.M., van Lengerich, B., and Boxer, S.G. (2009). Effects of linker sequences on vesicle fusion mediated by lipid-anchored DNA oligonucleotides. Proc. Natl. Acad. Sci. USA 106, 979–984.

Chang, V.T., Fernandes, R.A., Ganzinger, K.A., Lee, S.F., Siebold, C., McColl, J., Jönsson, P., Palayret, M., Harlos, K., Coles, C.H., et al. (2016). Initiation of T cell signaling by CD45 segregation at 'close contacts'. Nat. Immunol. 17, 574–582.

Chen, L., and Flies, D.B. (2013). Molecular mechanisms of T cell co-stimulation and co-inhibition. Nat. Rev. Immunol. 13, 227–242.

Choudhuri, K., Wiseman, D., Brown, M.H., Gould, K., and van der Merwe, P.A. (2005). T-cell receptor triggering is critically dependent on the dimensions of its peptide-MHC ligand. Nature 436, 578–582.

Daniels, D.S., Mol, C.D., Arvai, A.S., Kanugula, S., Pegg, A.E., and Tainer, J.A. (2000). Active and alkylated human AGT structures: a novel zinc site, inhibitor and extrahelical base binding. EMBO J. 19, 1719–1730.

Davis, M.M., Boniface, J.J., Reich, Z., Lyons, D., Hampl, J., Arden, B., and Chien, Y. (1998). Ligand recognition by alpha beta T cell receptors. Annu. Rev. Immunol. 16, 523–544.

Davis, S.J., and van der Merwe, P.A. (1996). The structure and ligand interactions of CD2: implications for T-cell function. Immunol. Today 17, 177–187.

Davis, S.J., and van der Merwe, P.A. (2006). The kinetic-segregation model: TCR triggering and beyond. Nat. Immunol. *7*, 803–809.

Douglass, E.F., Jr., Miller, C.J., Sparer, G., Shapiro, H., and Spiegel, D.A. (2013). A comprehensive mathematical model for three-body binding equilibria. J. Am. Chem. Soc. *135*, 6092–6099.

Dushek, O., and van der Merwe, P.A. (2014). An induced rebinding model of antigen discrimination. Trends Immunol. *35*, 153–158.

Edelstein, A., Amodaj, N., Hoover, K., Vale, R., and Stuurman, N. (2010). Computer control of microscopes using μManager. Curr. Protoc. Mol. Biol. *Chapter 14*, Unit14.20.

Eshhar, Z., Waks, T., Gross, G., and Schindler, D.G. (1993). Specific activation and targeting of cytotoxic lymphocytes through chimeric single chains consisting of antibody-binding domains and the gamma or zeta subunits of the immunoglobulin and T-cell receptors. Proc. Natl. Acad. Sci. USA *90*, 720–724.

Farlow, J., Seo, D., Broaders, K.E., Taylor, M.J., Gartner, Z.J., and Jun, Y.-W. (2013). Formation of targeted monovalent quantum dots by steric exclusion. Nat. Methods *10*, 1203–1205.

Gascoigne, N.R., Zal, T., and Alam, S.M. (2001). T-cell receptor binding kinetics in T-cell development and activation. Expert Rev. Mol. Med. *2001*, 1–17.

Grakoui, A., Bromley, S.K., Sumen, C., Davis, M.M., Shaw, A.S., Allen, P.M., and Dustin, M.L. (1999). The immunological synapse: a molecular machine controlling T cell activation. Science *285*, 221–227.

Gross, G., Gorochov, G., Waks, T., and Eshhar, Z. (1989). Generation of effector T cells expressing chimeric T cell receptor with antibody type-specificity. Transplant. Proc. *21*, 127–130.

Hopfield, J.J. (1974). Kinetic proofreading: a new mechanism for reducing errors in biosynthetic processes requiring high specificity. Proc. Natl. Acad. Sci. USA *71*, 4135–4139.

Hu, J., Lipowsky, R., and Weikl, T.R. (2013). Binding constants of membrane-anchored receptors and ligands depend strongly on the nanoscale roughness of membranes. Proc. Natl. Acad. Sci. USA *110*, 15283–15288.

Huang, J., Brameshuber, M., Zeng, X., Xie, J., Li, Q.-J., Chien, Y.-H., Valitutti, S., and Davis, M.M. (2013). A single peptide-major histocompatibility complex ligand triggers digital cytokine secretion in CD4(+) T cells. Immunity *39*, 846–857.

Huppa, J.B., Axmann, M., Mörtelmaier, M.A., Lillemeier, B.F., Newell, E.W., Brameshuber, M., Klein, L.O., Schütz, G.J., and Davis, M.M. (2010). TCR-peptide-MHC interactions in situ show accelerated kinetics and increased affinity. Nature *463*, 963–967.

Irving, B.A., and Weiss, A. (1991). The cytoplasmic domain of the T cell receptor zeta chain is sufficient to couple to receptor-associated signal transduction pathways. Cell *64*, 891–901.

James, J.R., and Vale, R.D. (2012). Biophysical mechanism of T-cell receptor triggering in a reconstituted system. Nature *487*, 64–69.

James, J.R., White, S.S., Clarke, R.W., Johansen, A.M., Dunne, P.D., Sleep, D.L., Fitzgerald, W.J., Davis, S.J., and Klenerman, D. (2007). Single-molecule level analysis of the subunit composition of the T cell receptor on live T cells. Proc. Natl. Acad. Sci. USA *104*, 17662–17667.

Janeway, C.A., Jr. (1995). Ligands for the T-cell receptor: hard times for avidity models. Immunol. Today *16*, 223–225.

Kaizuka, Y., Douglass, A.D., Varma, R., Dustin, M.L., and Vale, R.D. (2007). Mechanisms for segregating T cell receptor and adhesion molecules during immunological synapse formation in Jurkat T cells. Proc. Natl. Acad. Sci. USA *104*, 20296–20301.

Kamentsky, L., Jones, T.R., Fraser, A., Bray, M.-A., Logan, D.J., Madden, K.L., Ljosa, V., Rueden, C., Eliceiri, K.W., and Carpenter, A.E. (2011). Improved structure, function and compatibility for CellProfiler: modular high-throughput image analysis software. Bioinformatics *27*, 1179–1180.

Klammt, C., Novotná, L., Li, D.T., Wolf, M., Blount, A., Zhang, K., Fitchett, J.R., and Lillemeier, B.F. (2015). T cell receptor dwell times control the kinase activity of Zap70. Nat. Immunol. *16*, 961–969.

Krobath, H., Różycki, B., Lipowsky, R., and Weikl, T.R. (2009). Binding cooperativity of membrane adhesion receptors. Soft Matter *5*, 3354.

Lillemeier, B.F., and Davis, M.M. (2011). Probing the plasma membrane structure of immune cells through the analysis of membrane sheets by electron microscopy. Methods Mol. Biol. *748*, 169–182.

Liu, B., Chen, W., Evavold, B.D., and Zhu, C. (2014). Accumulation of dynamic catch bonds between TCR and agonist peptide-MHC triggers T cell signaling. Cell *157*, 357–368.

Malissen, B., and Bongrand, P. (2015). Early T cell activation: integrating biochemical, structural, and biophysical cues. Annu. Rev. Immunol. *33*, 539–561.

Manz, B.N., Jackson, B.L., Petit, R.S., Dustin, M.L., and Groves, J. (2011). T-cell triggering thresholds are modulated by the number of antigen within individual T-cell receptor clusters. Proc. Natl. Acad. Sci. USA *108*, 9089–9094.

McKeithan, T.W. (1995). Kinetic proofreading in T-cell receptor signal transduction. Proc. Natl. Acad. Sci. USA *92*, 5042–5046.

Mor, A., Campi, G., Du, G., Zheng, Y., Foster, D.A., Dustin, M.L., and Philips, M.R. (2007). The lymphocyte function-associated antigen-1 receptor costimulates plasma membrane Ras via phospholipase D2. Nat. Cell Biol. *9*, 713–719.

Murphy, M.C., Rasnik, I., Cheng, W., Lohman, T.M., and Ha, T. (2004). Probing single-stranded DNA conformational flexibility using fluorescence spectroscopy. Biophys. J. *86*, 2530–2537.

O'Donoghue, G.P., Pielak, R.M., Smoligovets, A.A., Lin, J.J., and Groves, J.T. (2013). Direct single molecule measurement of TCR triggering by agonist pMHC in living primary T cells. eLife *2*, e00778.

Ohashi, P.S., Mak, T.W., Van den Elsen, P., Yanagi, Y., Yoshikai, Y., Calman, A.F., Terhorst, C., Stobo, J.D., and Weiss, A. (1985). Reconstitution of an active surface T3/T-cell antigen receptor by DNA transfer. Nature *316*, 606–609.

Qi, S.Y., Groves, J.T., and Chakraborty, A.K. (2001). Synaptic pattern formation during cellular recognition. Proc. Natl. Acad. Sci. USA *98*, 6548–6553.

Reth, M. (2001). Oligomeric antigen receptors: a new view on signaling for the selection of lymphocytes. Trends Immunol. *22*, 356–360.

Sadelain, M., Brentjens, R., and Rivière, I. (2013). The basic principles of chimeric antigen receptor design. Cancer Discov. *3*, 388–398.

Schamel, W.W.A., Arechaga, I., Risueño, R.M., van Santen, H.M., Cabezas, P., Risco, C., Valpuesta, J.M., and Alarcón, B. (2005). Coexistence of multivalent and monovalent TCRs explains high sensitivity and wide range of response. J. Exp. Med. *202*, 493–503.

Schindelin, J., Arganda-Carreras, I., Frise, E., Kaynig, V., Longair, M., Pietzsch, T., Preibisch, S., Rueden, C., Saalfeld, S., Schmid, B., et al. (2012). Fiji: an open-source platform for biological-image analysis. Nat. Methods *9*, 676–682.

Selden, N.S., Todhunter, M.E., Jee, N.Y., Liu, J.S., Broaders, K.E., and Gartner, Z.J. (2012). Chemically programmed cell adhesion with membrane-anchored oligonucleotides. J. Am. Chem. Soc. *134*, 765–768.

Springer, T.A. (1990). Adhesion receptors of the immune system. Nature *346*, 425–434.

Stefanová, I., Dorfman, J.R., and Germain, R.N. (2002). Self-recognition promotes the foreign antigen sensitivity of naive T lymphocytes. Nature *420*, 429–434.

Stefanová, I., Hemmer, B., Vergelli, M., Martin, R., Biddison, W.E., and Germain, R.N. (2003). TCR ligand discrimination is enforced by competing ERK positive and SHP-1 negative feedback pathways. Nat. Immunol. *4*, 248–254.

Szymczak-Workman, A.L., Vignali, K.M., and Vignali, D.A.A. (2012). Design and construction of 2A peptide-linked multicistronic vectors. Cold Spring Harb. Protoc. *2012*, 199–204.

van der Merwe, P.A., and Dushek, O. (2011). Mechanisms for T cell receptor triggering. Nat. Rev. Immunol. *11*, 47–55.

Varma, R., Campi, G., Yokosuka, T., Saito, T., and Dustin, M.L. (2006). T cell receptor-proximal signals are sustained in peripheral microclusters and terminated in the central supramolecular activation cluster. Immunity *25*, 117–127.

Wallace, V.A., Penninger, J., and Mak, T.W. (1993). CD4, CD8 and tyrosine kinases in thymic selection. Curr. Opin. Immunol. *5*, 235–240.

Williams, B.L., Schreiber, K.L., Zhang, W., Wange, R.L., Samelson, L.E., Leibson, P.J., and Abraham, R.T. (1998). Genetic evidence for differential coupling of Syk family kinases to the T-cell receptor: reconstitution studies in a ZAP-70-deficient Jurkat T-cell line. Mol. Cell. Biol. *18*, 1388–1399.

Wülfing, C., Sumen, C., Sjaastad, M.D., Wu, L.C., Dustin, M.L., and Davis, M.M. (2002). Costimulation and endogenous MHC ligands contribute to T cell recognition. Nat. Immunol. *3*, 42–47.

Yin, J., Lin, A.J., Golan, D.E., and Walsh, C.T. (2006). Site-specific protein labeling by Sfp phosphopantetheinyl transferase. Nat. Protoc. *1*, 280–285.

Zadeh, J.N., Steenberg, C.D., Bois, J.S., Wolfe, B.R., Pierce, M.B., Khan, A.R., Dirks, R.M., and Pierce, N.A. (2011). NUPACK: Analysis and design of nucleic acid systems. J. Comput. Chem. *32*, 170–173.

Zhang, D.Y., Turberfield, A.J., Yurke, B., and Winfree, E. (2007). Engineering entropy-driven reactions and networks catalyzed by DNA. Science *318*, 1121–1125.

STAR★METHODS

KEY RESOURCES TABLE

REAGENT or RESOURCE	SOURCE	IDENTIFIER
Antibodies		
Mouse anti-CD69 conjugated to Alexa647 (FN50)	Thermo Fisher Scientific	Cat#: MA5-18150; RRID: AB_2539524
anti-phosphoERK (rabbit polyclonal)	Cell Signaling Technology	Cat#: 9101; RRID:AB_331646
Chemicals, Peptides, and Recombinant Proteins		
His10-SNAPf-ybbr13	This study	
His10-CLIPf-ybbr13	This study	
Latrunculin A	Sigma	Cat#: L5163-100UG
BC-GLA-NHS	New England Biolabs	Cat#: S9237S
BG-GLA-NHS	New England Biolabs	Cat#: S9151S
Puromycin dihydrochloride	Sigma	Cat#: P8833-10MG
Experimental Models: Cell Lines		
Human: JRT3	Art Weiss; Ohashi et al., 1985	
Human: JRT3 expressing DNA-CARζ-GFP	This study	
Human: JRT3 expressing DNA-CARζ-GFP/ZAP70-mCherry	This study	
Human: JRT3 expressing DNA-CARζ-IRESpuro/ZAP70-GFP	This study	
Human: JRT3 expressing DNA-CARζ-IRESpuro/ZAP70-GFP	This study	
Human: JRT3 expressing DNA-CAR$_{TCR}$/ZAP70-GFP	This study	
Human: P116	Art Weiss; Williams et al., 1998	
Human: P116 expressing DNA-CARζ-IRESpuro/ZAP70-GFP	This study	
Human: HEK293T	ATCC	Cat#: CRL-3216
Recombinant DNA		
pHR-DNA-CARζ-GFP	This study	
pHR-DNA-CARζ-IRESpuro	This study	
pHR-SP-SNAPf:TCRβ-IRESpuro	This study	
pHR-TCRα-E2A-SNAPf:TCRβ-P2A-CD3ε-P2A-CD3ζ	This study	
pHR-ZAP70-GFP	James and Vale, 2012	
pHR-ZAP70-mCherry	James and Vale, 2012	
Oligonucleotides		
A full list of oligonucleotides is presented in Table S1.	N/A	N/A
Software and Algorithms		
GraphPad Prism v6	GraphPad	http://www.graphpad.com/scientific-software/prism/
MATLAB	Mathworks	https://www.mathworks.com/
vbFRET	Bronson et al., 2009	http://vbfret.sourceforge.net/
FIJI	NIH	https://fiji.sc/
Cell Profiler 2.1.1	The Broad Institute	http://cellprofiler.org/
μManager	Open Imaging	https://open-imaging.com/
C script to analyze stochastic signaling model	This study	https://github.com/kabirhusain/mjtayloretal_clustergillespie

CONTACT FOR REAGENT AND RESOURCE SHARING

Further information and requests for resources and reagents should be directed to Lead Contact Ron Vale (ron.vale@ucsf.edu).

EXPERIMENTAL MODEL AND SUBJECT DETAILS

Cell Culture

JRT3 Jurkat cells (which fail to express the TCR; Ohashi et al., 1985) and P116 Jurkat cells (which do not express ZAP70; Williams et al., 1998) were kindly provided by Art Weiss (UCSF). Both cell lines were grown in RPMI (Invitrogen) with 10% FBS (Invitrogen) supplemented with 2 mM L-glutamine. HEK293T cells (purchased from the ATCC collection) were grown in DMEM (Invitrogen) supplemented with 2 mM L-glutamine. All cells were determined to be negative for mycoplasma using the MycoAlert detection kit (Lonza).

METHOD DETAILS

Generation of DNA-CARs and ZAP70 Constructs

Two versions of the DNA-CARζ were constructed: 1) DNA-CARζ with a C-terminal cytoplasmic monomeric eGFP (herein termed "GFP") (pHR-DNA-CARζ-GFP), and 2) a non-fluorescent alternate version with a N-terminal HA epitope tag (YPYDVPDYA). The HA tag was inserted to allow cell surface expression levels to be monitored via FACS. Apart from the addition of a HA tag or GFP in these two versions, the receptor was otherwise identical. All primers were purchased from Integrated DNA Technology, and primers longer that 60 nucleotides were ordered as Ultramer oligos. Full details of the construction of the DNA-CARζ and DNA-CAR$_{TCR}$ are given below.

DNA-CARζ-GFP

To construct DNA-CARζ-GFP, the human CD3ζ cytoplasmic tails (aa 58-164) fused to the transmembrane domain of CD86 (aa 236-271) was amplified by polymerase chain reaction. The template used for this PCR was a CD86-CD3ζ chimeric receptor previously described (James and Vale, 2012)). This produced a DNA fragment with a 5′ 3x gly-gly-ser linker and 3′ BamH1 restriction site. A second PCR amplified SNAPf (from the pSNAPf plasmid, New England Biolabs) with a N-terminal signal peptide (MQSGTHWRVLGLCLLSVGVWGQD) derived from CD3ε. This PCR also introduced a 5′ Mlu1 restriction site and 3′ 3x gly-gly-ser linker (complementary to the first PCR product). A stitch PCR was then set up to produce a final PCR product that was digested with Mlu1 and BamH1 and ligated in frame with mGFP in the second-generation pHR-mGFP lentiviral vector.

DNA-CARζ-IRESpuro

DNA-CARζ-IRESpuro was constructed using DNA-CARζ-GFP as PCR template. An IDT Ultramer forward primer was designed so that a HA epitope tag was inserted between the signal peptide and the SNAPf open reading frame. This version of the DNA-CARζ was digested with Mlu1 and BamH1 and ligated into a pHR lentiviral vector that had a downstream IRES-puromycin resistance cassette (pHR-DNA-CARζ-IRES-puro).

DNA-CAR$_{TCR}$-IRESpuro

DNA-CAR$_{TCR}$ was constructed using the Jurkat TCRβ open reading frame as a template. A primer was designed to PCR amplify a DNA fragment consisting of signal peptide fused SNAPf with a 5′ Mlu1 site and 3′ gly-ser-gly-ser linker (this PCR used DNA-CAR as a template). A second set of primers were designed to PCR amplified the Jurkat TCRβ open reading frame (omitting the signal peptide) with 5′ portion of SNAPf ORF and gly-ser-gly-ser linker (complementary to the first PCR product) and a 3′ BamH1 site. A stitch PCR was then set up to produce a final PCR product (signal peptide-SNAPf-TCRβ) that was digested with Mlu1 and BamH1 and ligated into a pHR lentiviral vector that had a downstream IRES-puromycin resistance cassette (pHR- DNA-CAR$_{TCR}$-IRESpuro).

pHR-TCRα-E2A-SNAPf:TCRβ-P2A-CD3ε-P2A-CD3ζ

To overcome low surface expression of DNA-CAR$_{TCR}$ (see Cell Culture and Reagents, below) a vector was constructed to increase expression of additional Jurkat TCR subunits. We created a multicistronic lentiviral vector where multiple TCR subunits and the SNAPf:TCRβ were separated by 2A "ribosome skip" peptides (Szymczak-Workman et al., 2012). DNA fragments of each of the Jurkat TCR subunits were PCR amplified with primers that added either the E2A or P2A peptide sequences at the 5′ and 3′ terminus. PCR also generated fragments with 15-20 bp overlaps at the 5′ and 3′. The pHR lentiviral vector was digested with Mlu1 and Not1. DNA fragments were combined with digested vector and assembled using Gibson Assembly cloning.

ZAP-GFP

pHR-ZAP70-GFP and pHR-ZAP70-mCherry were as described earlier (James and Vale, 2012).

Lentiviral Production and Generation of Stable Expressing JRT3 Cell Lines

Lentivirus particles were produced in HEK293T cells by co-transfection of the pHR transfer plasmids with second generation packaging plasmids pMD2.G and psPAX2 (a gift from Didier Trono, Addgene plasmid # 12259 and # 12260). Virus particles were harvested from the supernatant after 48-72 hr, filtered and applied to JRT3 cells overnight. The next day the cells were resuspended in fresh RPMI media and recovered for 3 days. DNA-CARζ-GFP expressing JRT3 cells were FACS sorted to generate a stable and

homogeneous expressing population. JRT3 transduced with pHR-DNA-CARζ-IRES-puro/pHR-DNA-CAR$_{TCR}$-IRESpuro were selected at 4 μg/ml of puromycin (Sigma) and maintained with 2 μg/ml of puromycin.

FACs analysis of DNA-CAR$_{TCR}$ expressing JRT3 cells revealed low surface expression (as compared to wild-type E6.1 Jurkats) of the full TCR complex, despite puromycin selection. To increase plasma membrane expression, JRT3 cells were subsequently transduced with pHR-TCRα-E2A-SNAPf:TCRβ-P2A-CD3ε-P2A-CD3ζ to enhance the expression of additional TCR subunits. Second, to selectively sort for cells with high surface expression levels of DNA-CAR$_{TCR}$, JRT3 cells were labeled with SNAP-Surface-647 (NEB) and sorted by FACS. This resulted in a population with a plasma membrane expression level of DNA-CAR$_{TCR}$ that was comparable to wild-type Jurkats TCR levels (as compared by FACS analysis).

Imaging Chambers and Supported Lipid Bilayers

Phospholipid mixtures consisting of 97.5% mol 1-palmitoyl-2-oleoyl-*sn*-glycero-3-phosphocholine (POPC), 2% mol 1,2-dioleoyl-sn-glycero-3-[(N-(5- amino-1-carboxypentyl) iminodiacetic acid) succinyl] (nickel salt) (Ni^{2+}⁻NTA-DOGS) and 0.5% mol 1,2-dioleoyl-sn-glycero-3- phosphoethanolamine-N-[methoxy(polyethylene glycol)-5000] (PE-PEG5000) were mixed in glass vials and dried down under argon. All lipids used were purchased from Avanti Polar Lipids. Dried lipids were placed under vacuum for 2 hr to remove trace chloroform and resuspended in PBS. Small unilamellar vesicles were produced by several freeze-thaw cycles. Once the suspension had cleared, the lipids were spun in a bench top ultracentrifuge at 65,000xg for 45 min and kept at 4°C for up to 5 days.

Supported lipid bilayers were formed in 96-well glass bottom plates (Matrical), which were cleaned by extensive rinsing in isopropanol following by water. Plates were then cleaned for 15 min with a 1% Hellmanex solution heated to 50°C followed by extensive washing with pure water. 96 well plates were dried with nitrogen and sealed until needed. To prepare SLB, individual wells were cut out and base etched for 5 min with 5 M KOH and then washed with water and finally PBS. SUVs suspension were then deposited in each well and allowed to form for 1 hr. We found that SUVs suspension containing 0.5% mol PE-PEG5000 formed best at 37°C. After 1 hr, wells were washed extensively with PBS. SLBs were incubated for 15 min with HEPES buffered saline (HBS: 20 mM HEPES, 135 mM NaCl, 4 mM KCl, 10 mM glucose, 1 mM CaCl$_2$, 0.5 mM MgCl$_2$) containing 1% BSA to block the surface and minimize non-specific protein adsorption. After blocking, the SLB were functionalized by incubation for 1 hr with his-tagged proteins. The labeling solution was then washed out and each well was completely filled with HBS with 1% BSA. Total well volume was 625 μl (manufacturers specifications), and 525 μl was removed leaving 100 μl of HBS 1% BSA in each well.

Protein Expression, Purification, and Labeling

SNAPf and CLIPf open reading frames were cloned into a pET28a vector containing a N-terminal 10X His tag. A C-terminal ybbr13 tag (DSLEFIASKLA) (Yin et al., 2006) was added by PCR. Proteins were expressed in BL21-DE3 *E. coli* and purified by Ni-NTA resin followed by gel filtration. Ybbr13 peptide labeling was performed using CoA-Atto647N as described (Yin et al., 2006). The degree of labeled was calculated with a spectrophotometer by comparing 280nm and 640 nm absorbance (usually 85%–95% labeling efficiency was achieved).

Synthesis of Benzylguanine-Conjugated DNA Oligonucleotides

All receptor/ligand/adhesion oligonucleotides were ordered from IDT with a 3′/5′ terminal amine. Conjugation to benzyl-guanine or benzyl-cytosine was performed as described (Farlow et al., 2013). 10x His tagged SNAP and CLIP were labeled with benzlyguanine/benzylcytosine DNA on the same day SLBs were prepared. SNAP/CLIP were labeled at a concentration of 5 μM with a 3-fold excess of BG/BC-DNA in 20 mM HEPES (pH 7.4) 200 mM NaCl and 1 mM TCEP. DNA-SNAP/CLIP linkage was monitored by mobility shift assays using SDS-PAGE. Maximal labeling was achieved after 40 min at room temperature (~90% labeling efficiency).

DNA Ligand and Receptor Sequence Design

We selected a 16-nucleotide DNA strand that had no discernable secondary structure (as measured using nupack.org [Zadeh et al., 2011], accessed between 12/2012 and 06/2013) and have been previously characterized (Zhang et al., 2007). The free energy of DNA hybridization for each DNA ligand was calculated with nupack.org using input parameters of 37°C with 150 mM NaCl and 2.5 mM MgCl$_2$. The receptor/ligand 16-mer DNA strand had the following sequences: ligand (5′-CCACATACATCATATT-3′; ΔG = −15.85 kcal/mol) and receptor (5′-AATATGATGTATGTGG-3′). All receptor/ligand DNA strands were ordered from Integrated DNA Technology with 3′ amine functional group. Truncations of the initial 16-mer DNA ligand sequence were generated from the 5′ end. To maintain the overall length of the DNA ligand as presented on the SLB, a poly-thymine spacer was added back at the 3′ end. The truncation ligands had the following sequence: 13-mer ligand (5′- CATACATCATATTTTT-3′; ΔG = −12.16 kcal/mol), 12-mer ligand (5′- ATACATCATATTTTTT-3′; ΔG = −10.73 kcal/mol), and 11-mer ligand (5′- TACATCATATTTTTTT-3′; ΔG = −10.14 kcal/mol). For experiments using shorter complementary DNA ligands the same 16-mer DNA receptor sequence was used (5′-AATATGATGTATGTGG-3′). Mutant versions of the 11-mer were generated by sequential addition of C/G base pairs. Mutant 11-mer strands were analyzed by nupack.org to minimize secondary structure. The following mutant 11-nucleotide DNA receptor-ligand pairs were used (mutations underlined): DNA receptor (5′-AAT<u>G</u>TGATGTATTTTT-3′), DNA ligand (5′-TACATCA<u>C</u>ATTTTTTT-3′; ΔG = −11.86 kcal/mol), DNA receptor (5′-AA<u>GG</u>TGATGTATTTTT-3′), DNA ligand (5′-TACATCA<u>CC</u>TTTTTTT-3′; ΔG = −12.65 kcal/mol), DNA receptor (5′- AA<u>GG</u>TGA<u>G</u>GTATTTTT-3′), and DNA ligand (5′-TAC<u>C</u>TCA<u>CC</u>TTTTTTT-3′; ΔG = −13.44 kcal/mol).

The triggerable DNA signaling system used the following 16-mer DNA receptor sequence (5′-CCACATACATCATATT-3′), and the SLB was functionalized with a 20-mer non-complementary DNA ligand (5′- CCCTCATTCAATACCCTAGG-3′). In this system the 20-mer DNA ligand was ordered from Integrated DNA Technology with 5′ amine functional group and labeled with BC-NHS as described above. Receptor and ligand were brought together by the addition of an oligo with complementary regions to both receptor and ligand (5′-AATATGATGTATGTGGttCCTAGGGTATTGAATGAGGG-3′). The addition of trigger strand results in a 36 base pair overlap. While this trigger strand system was useful for investigating kinetics by synchronizing the timing of ligand-receptor interaction, the complexity of this three-component binding interaction system (Douglass et al., 2013) made it difficult to use for generating ligand dose responses.

The kinetic segregation hypothesis states that the inter-membrane spacing distance is important for the exclusion of CD45 and signal transduction (Davis and van der Merwe, 2006). In Figure 2B, we note that there may be subtle changes in overall length between the 16-mer ligand-receptor duplex and the 11-mer ligand-receptor duplex with overhang of 5 nucleotides of single-stranded DNA. Single-stranded DNA obeys a worm-like chain model (Murphy et al., 2004) and thus has a much smaller persistence length (∼2-3 nm in physiological salt) compared to the 50 nm persistence length for double-stranded DNA. Thus, in the absence of other forces, a change from ds to ssDNA should decrease inter-membrane distance for entropic reasons. However, counteracting forces (e.g., the microenvironment of the glycocalyx or other forces from membrane bending) might place the system under tension and could extend and stretch ssDNA. Regardless, the length difference between 5 bp of dsDNA and 10 bases of extended or compacted ssDNA is likely to be modest. If the ssDNA is entropically compacted, then the intermembrane distance of the 11-mer may be similar or slightly decreased compared to the 16-mer. If fully extended, then the intermembrane distance could increase by a maximum of 3.5 nm. The predicted 16-mer ligand-receptor dimension is estimated at 13 nm (see Results) and thus this uncertainty or variation in membrane spacing is unlikely to change the general conclusions that receptor-ligand binding energy affects the dose response curve of T cell signaling (Figure 2B). We note also that Figure 2C varies binding energy without any potential for length change.

DNA-Based Adhesion System
The 100-mer adhesion strand used in this study consisted of a 3′ 20-mer complementary region (5′- ACTGACTGACTGACTGACTG-3′) attached through a 80-mer poly-dT linker to a lipid anchor (1,2-O-Dihexadecyl-sn-glycerol) via a phosphodiester linkage at the 5′ end. Dialkylglycerol phosphoramidites were synthesized as previously described (Chan et al., 2009; Selden et al., 2012). The complementary sequence (5′- CAGTCAGTCAGTCAGTCAGT-3′) was ordered from Integrated DNA Technology with a 5′ amine and labeled with BG-NHS as previously described above. This strand was then conjugated to His10-SNAPf to label SLBs. Cells were labeled with the DNA adhesion lipid molecule for 3 min at room temperature at a labeling concentration of 5 μM (stock concentration of 250 μM).

BG-DNA Labeling of JRT3 Cells Expressing DNA-CAR
JRT3 cells expressing DNA-CARζ/DNA-CAR$_{TCR}$ were spun down, re-suspended in HBS and incubated with 5 μM of BG-DNA receptor for 30 min at room temperature. Cells were conjugated with BG-DNA at an approximate density of 2×10^7 cells/ml. During conjugation cells were maintained in suspension by gently agitation. DNA adhesion lipid was added during the final 3 min of labeling. Cells were washed twice in HBS before being used.

CD69 Expression
To assay CD69 expression by FACS, supported lipid bilayer were set up on 7 μm silica beads (Bangs Laboratories). Silica beads were counted using a hemocytometer mixed with 2.5×10^5 JRT3 cells expression DNA-CARζ-GFP in 96 well plates in a 3:1 ratio of bead to cells. Signaling was initiated by the addition of DNA trigger strand. A portion of cells were also plated onto poly-L-lysine containing coverslips and analyzed by spinning disk confocal to inspect SLB quality and confirm cellular activation via re-localization of DNA-CARζ-GFP to the bead-cell interface after addition of the trigger DNA strand (Figure S1C). 4 hr after activation cells were pelleted and re-suspended in PBS with 2% (v/v) fetal bovine serum and 0.1% (w/v) NaN₃. Cells were labeled with mouse anti-CD69 conjugated to Alexa647 (FN50, Thermo Fisher Scientific, 10 μg/ml) for 1 hr on ice. Cells were washed twice and then fixed. Cells were then run on a LSRII (Becton Dickinson) (10,000 gated cells analyzed).

Calcium Imaging and Analysis
Calcium signaling assay was performed on JRT3 cells pre-incubated with 10 μM fura-2 (Invitrogen) for 30 min. Ratiometric fura-2 imaging (340 nm/380 nm excitation) was performed on a microscope (Nikon TE2000U) equipped with wavelength switcher (Sutter Instrument Co. Sutter Lambda XL lamp) and fura-2 excitation and emission filters. Images were projected on to Photometric CoolSNAP HQ2 CCD camera using an S Fluor 40X 1.3 NA oil objective. JRT3 cells expressing DNA-CARζ-GFP were pipetted onto supported lipid bilayer incubated for 10 min to allow cells to settle and adhere to the SLB using the DNA adhesion system described. Cells were imaged for 1–2 min in a quiescent state before the addition of trigger strand to initiate signaling. Image analysis was performed in FIJI (Schindelin et al., 2012) by manually segmenting the cell outline and measuring the mean 340 nm/380 nm excitation ratio in the cell volume.

PhosphoERK Data Acquisition and Analysis

Titrations of ligand density on SLBs were set up using 96-well plates. For each phosphoERK assay, all SLB ligand densities were set up in triplicate. Ligand density was determined by maintaining identical labeling protein concentrations and time, but changing the portion of DNA-ligand labeled His10-CLIPf-Atto647N. Before application of cells, SLBs were analyzed by TIRF microscopy to check formation, mobility and uniformity. Short time series were collected at low ligand densities (e.g., $\geq$ 1 molecule per μm^2) to calculate ligand densities on the SLB based upon direct single molecule counting. Wells containing only DNA adhesion strands served as un-stimulated controls or used for phorbol 12-myristate 13-acetate stimulation.

On the day of an experiment JRT3 cells expressing DNA-CARζ-GFP were transferred to serum free media for several hr before being functionalized with BG-DNA receptor. After DNA functionalization cells were re-suspended in HBS at a final concentration of 2.5×10^5 cells per ml. 100 μL of cells (corresponding to 2.5×10^4 cells per well) were then applied to 96 plates wells using a multi-channel pipette (total well volume after addition of cell was 200 μl). Cells were then incubated at 37°C for 15 min before the addition of 200 μl of 2x fixative (7% (v/w) PFA with 1% (v/w) Triton X). Cells were fixed for 20 min at room temperature. Cells were then washed with PBS containing 60 mM glycine to quench PFA. Cells were then blocked in PBS 10% (w/v) BSA for 1 hr before addition of primary antibody. Cells were labeled over night with anti-phosphoERK (rabbit polyclonal, Cell Signaling Technology #9101, used at 1:500). The next day cells were washed 5X in PBS 10% (w/v) BSA, and labeled with goat anti-rabbit conjugated to Alexa555 (Invitrogen, used at 1:1000) for 1 hr. Finally cells were washed 5X in PBS. In the penultimate PBS wash, cells were labeled for 10 min with DAPI at a labeling concentration of 300 nM.

96-well plates were imaged on an inverted microscope (Nikon TiE, Tokyo, Japan) equipped with Lumencor Spectra-X illumination. Fluorescent images were acquired with Nikon plan apo 20X 0.75 NA air objective lens and projected on an Andor Zyla 5.2 camera with 2x2 binning (pixel size 425nm) and a 1.5x magnification lens. The fluorescent emission was collected through filters for EGFP (525 $\pm$ 30nm), Alexa 555 (607 $\pm$ 36nm) and DAPI (440 $\pm$ 40). Image acquisition was performed using MicroManager software (Edelstein et al., 2010). Each well was imaged using the Create Grid plugin in the MicroManager multidimensional acquisition GUI. The Create Grid plugin was used to automate the acquisition of the entire well. A dark image was subtracted from each image during acquisition using the Multi-channel shading MicroManager plugin.

Imaging Single Ligand-Receptor Dwell Time

Single molecule measurements of receptor-ligand dwell time were performed on an inverted microscope (Nikon TiE,Tokyo, Japan) equipped with a spinning disk confocal and TIRF combined system (Spectral Diskovery, Ontario, Canada). Two color simultaneous TIRF laser illumination with 488 and 638 nm was provided by directly modulated lasers combined into a two fiber output (Spectral ILE, Ontario, Canada). Following the general methodology of O'Donoghue et al. (O'Donoghue et al., 2013), single molecule TIRF measurements were imaged in streaming mode with a 500 ms exposure time to detect the bound fraction of ligand on the supported lipid bilayer. By using a 500 ms exposure, the bound ligands were detected as discrete spots of fluorescence intensity due to relatively slow diffusion of receptor-bound ligands; unbound ligands on the supported lipid diffused much faster and created a background blurred image on the camera detector (see Figures S2C and S2D). Fluorescent emissions of GFP (receptor) and Atto647N (ligand) were split using a 650 nm long pass dichroic onto two Andor iXon Ultra EMCCDs (Belfast, Ireland). Illumination was controlled using digital control boards (Arduino Uno, Turin, Italy) and triggers from the cameras. Image acquisition was performed using MicroManager software (Edelstein et al., 2010). A standard constant temperature of 37°C was maintained using an OKO Labs stage top incubator.

Imaging and Analysis of Single Ligand-Receptor Interactions and ZAP70 Recruitment

Imaging of ZAP70-GFP recruitment was performed on an inverted microscope (Nikon TiE, Tokyo, Japan) equipped with NIKON fiber launch TIRF illuminator. Illumination was controlled with an Agilent Laser combiner using the 488 and 640 nm laser lines at approximately 0.1 and 0.05 mW laser power respectively. Fluorescence emission was collected through filters for GFP (525 $\pm$ 25 nm) and Atto647N (700 $\pm$ 75 nm). All images were collected using a Nikon Plan Apo 100x 1.4 NA oil-immersion objective that projected onto a Photometrics Evolve EM-CCD camera with a calculated pixel size of 103 nm. A constant temperature of 37°C was maintained using a Tokai Hit stage top incubator.

JRT3 cells expressing DNA-CARζ or DNA-CAR$_{TCR}$ (under puromycin selection) and ZAP70-GFP were pipetted onto supported lipids bilayers functionalized with His10-CLIPf-Atto647N conjugated to DNA ligand. JRT3 cells and SLBs were sequentially illuminated for 500 ms with 488 nm and 640 nm laser lines. Diffraction-limited punctae of Atto647N representing bound DNA ligands were detected and tracked using Trackmate FIJI plugin as described above. A hidden Markov Model (HMM) analysis was then used to identify the number of fluorescent ligands in each frame from the fluorescence intensity of a tracked Atto647N ligand cluster. The same analysis was also used to detect the moment ZAP70 was recruitment to a DNA ligand microcluster. The HMM analysis implemented in this study was the statistical maximum evidence approach described previously by Bronson et al. (Bronson et al., 2009) (see Figure S3 and below).

To analyze ligand on rate, we segmented the cells-SLB interface using the ZAP70-GFP fluorescence by applying a threshold using FIJI. We calculated the cell-SLB interface surface area from the threshold image and using the Analyze Particle plugin, and calculated the median surface area during the initial 3 min of the cell landing on the SLB. We used this to calculate a ligand binding on-rate based on cell-SLB interface area and the number of de novo single molecule events detected in this 3 min window. We calculated the ligand

on-rate in clusters by scoring new binding events that occurred after the initial single molecule binding event that seeded that receptor-ligand cluster. The time interval was calculated from the molecule binding event that preceded the subsequent binding event (e.g the time interval between the second and third binding event). Micro-cluster area was estimated as a diffraction limit spot (calculated using a spot with 0.2 μm radius – radius^2 x π). We only analyzed events where clear quantal steps were detected. In most examples this meant we could reliably analyze the second and third ligand binding events, but in some case we could analyze up to 5 binding event at an individual micro-cluster.

Construction of a Stochastic Signaling Model
Model Construction and Validation
The goal of our theoretical model was to quantitatively assess the degree of ligand discrimination provided by the experimentally observed mechanisms. This model considered a T cell interacting with a ligand functionalised supported lipid bilayer (Figure S7A) and the transitions that occur between single bound ligands and receptor-ligand clusters (Figures S7B and S7C) over a defined passage of time (fixed at 500 s). We fixed the parameters used in our theoretical model directly from the experimental measurements. These parameters were the following: k_b is the rate at which new ligand bound to a site consisting of a existing contact site (also the rate at which single receptor bounds ligands converted into clusters). This rate was taken to be proportional to the ligand concentration on the supported lipid bilayer. The constant of proportionality between k_b and the ligand concentration [L] was computed by extracting the value of k_b from the 16-mer data at 1 molecule per μm^2 data (Figure S7D). k_u is the unbinding rate of ligands, the inverse of which is the average dwell time τ_u, and was obtained from the single-molecule dwell-time data (Figures 2 and S2). k_0 is the rate at which receptors on the T cell surface bind to ligands on the SLB, forming a *contact site* between the cell and the supported lipid bilayer, referred to as "de novo binding" (Figure S7E). $k_z^{(off)}$ is the unbinding rate of ZAP70 estimated from the experimental data of ZAP70 dwell times at single ligands (Figure 3C). $k_z^{(on)}$ is the on rate of ZAP70 binding and was calculated by measuring the average time between contact site formation and initial ZAP70 recruitment (< T >, Figure S7F, left), and then inferring the corresponding value of $k_z^{(on)}$ (Figure S7F, right).

In principle, each DNA-CAR may bind three ZAP70 molecules (one at each ITAM on the CD3ζ cytoplasmic domain); however in this model, we make the simplifying assumption that each receptor is either ZAP70 positive or negative (congruent with our image analysis, Figure S3E). Kinetic proofreading arises from this model because ligand unbinding from a ZAP70-positive receptor results in the loss of both a ligand and a ZAP70-positive receptor from a contact site ($(n, m) \rightarrow (n-1, m-1)$, see state space in Figure S7B). This loss may only be reversed by two steps ($(n-1, m-1) \rightarrow (n, m-1)$ and $(n, m-1) \rightarrow (n, m)$, i.e., ligand binding followed by ZAP70 recruitment), thereby inducing a temporal delay and energetic cost that is the defining feature of kinetic proofreading (Hopfield, 1974). If all ligands unbind from a contact site, then that contact site ceases to exist (i.e., the cluster disassembles).

With all parameters fixed, we assess the validity of the model by quantitative comparisons of its predictions with experimental data. Here, we present three such comparisons:

- **Number of 16-mer Ligands at Initial ZAP70 Binding**: We plot the prediction of the theory (analytically calculated from the model) against the experimental data (Figure S7G) and observe an excellent agreement. Note that the data considered here only includes the 16-mer tracks that *do* recruit ZAP70.
- **Propensity of 16-mer Ligand Clusters to Stay ZAP70-free**: To analyze the ability of the model to understand all of the data, including those tracks that do not recruit ZAP70, we do the following: from the ligand channel of each contact site in the 16-mer dataset we compute the probability that the track *does not* recruit ZAP70 (using the assumptions and rates of the model) using Poisson statistics:

$$q = \exp\left(- k_z^{(on)}\tau_1 \right) \times \exp\left(- 2 k_z^{(on)}\tau_2 \right) \times \ldots \times \exp\left(- n k_z^{(on)}\tau_n \right) \times \ldots$$

where n is the length of time for which the contact site has exactly n ligated receptors.

We then bin contact sites by their q values (Figure S7H) we have used ten bins (0 → 0.1, 0.1 → 0.2 etc., plotted on the x axis). For the tracks in each bin, we then ask what fraction actually remains ZAP70-free - plotted on the y axis. We expect from the model that the data points would fall on the x = y diagonal (black line). We indeed find that the data-points lie close to the diagonal, tracking it very well, but lie consistently above it. This suggests that there is slightly less ZAP70 than expected, which could be due to the difficulty in detecting ZAP70 against the fluctuating fluorescent background, or the recruitment of non-fluorescent ZAP70.

- **13-mer Cluster "Stability"**: To validate our model in the context of a rapidly unbinding ligand, we look at the "lifetime" of a cluster of 13mers. To be more precise, we consider the amount of time for which the number of ligands at a contact site is n > 1. As the rate of ligand unbinding ($k_u \approx (1/60)s^{-1}$) is comparable to the rate of bleaching ($(1/30)s^{-1}$), we considered the bleaching-renormalized ligand 'unbinding' rate: 1/60 + 1/30 = $(1/20)s^{-1}$. The results (obtained from stochastic simulation of the model, Figure S7I) show an excellent agreement with experimental data.

Ligand Discrimination in the Model

We performed stochastic simulations of cells interacting with an SLB of ligand concentration [L] and off-time $\tau_u = 1/k_u$. At each point in parameter space, we simulated N = 250 cells for 500 s (chosen to match the experimental timescales); the time-series of (n, m) for each receptor-ligand contact site in each cell was then analyzed for the following potential *activation thresholds*:

- A minimum cluster size (e.g., number of ligated receptors within a cluster): $n_* = 4$, 8 or 16.
- A minimum number of ZAP70-positive receptors within a cluster: $m_* = 4$, 8 or 16.
- A minimum length of time for which a bound ligand or cluster has m > 0 ZAP70-positive receptors: $\tau[m] = 100$ s.

The rationale was to analyze how the emergence of these features correlated with the experimentally observed downstream signaling outputs of phosphoErk (evaluated as 20% phosphoERK activation threshold, Figures 2B and 2C). If a cell contained at least one contact site that satisfied the particular activation threshold within the simulation time of 500 s, the cell was scored as having satisfied that threshold criterion. We could then construct *heatmaps*, (as in Figure 7B), that assigned to each point in parameter space the fraction of cells that satisfied the threshold criterion, the 20% contour of which was used to demarcate boundaries of activation in parameter space (Figure 7C and Figures S7J–S7L). The results demonstrate how these activation thresholds can tune the sensitivity and specificity of ligand discrimination. We found that phospoERK signaling thresholds (Figures 2B and 2C) mapped to regions in the parameter space were the signaling model found larger clusters that stably recruited ZAP70 (Figures 7C and S7J). However by these criteria our model predicts that a 11-mer DNA ligand (TACATCATATT) with a ~2 s dwell time and no discernable signaling activity (Figures 2B and 2D) would have an affinity sufficient to activate phosphoERK at high ligand concentrations (~900–1000 ligand per μm^2, Figures S7J–S7K). This suggests that the degree of ligand discrimination of this model is lower than experimentally observed, and suggest of other possible mechanisms involved in discrimination.

We went on to analyze the effect of incorporating a 'cooperative switch' in ZAP-70 stability, defined as a change in the off-rate of ZAP70 from $k_z^{(off)}$ to $\varepsilon k_z^{(off)}$ ($\varepsilon < 1$, see schematic in Figure S7L) when the number of ligated receptors at a contact site crosses some threshold (here chosen as n > 2). We find (Figure S7L) that increasing the stability of ZAP70 results in an enhanced sensitivity for high affinity ligands (i.e., shifting the activation boundary for the m_* or $\tau[m]$ thresholds to lower [L] specifically for ligands with larger off-times τ_u).

Stochastic Simulation Method

Simulations were performed with the Gillespie stochastic simulation algorithm, implemented in custom C code, in two steps:

- De novo binding times i were generating using the rate k_0, between t = 0 and t = 500 s.
- For each of these, a Gillespie simulation was run on the state space in Figure S7B, starting in the state (1,0) at t = i
- Each contact site was simulated until one of three events occurred: (a) all ligated receptors unbind (n = 0), or (b) total simulation time t = 500 s was reached.

QUANTIFICATION AND STATISTICAL ANALYSIS

All data are expressed as the mean ± the standard deviation (SD) or mean ± the standard error of the mean (SEM), as stated in the figure legends and results. The exact value of n and what n represents (e.g., number of cells, single molecule ligand binding events or experimental replicates) is stated in figure legends and results.

PhosphoERK Quantification and Analysis

Image analysis of phosphoERK staining was performed using Cell Profiler (Kamentsky et al., 2011) and FIJI. Unsuitable images that had focus defects or fluorescent debris were discarded from the image series from each well. The Alexa555 channel, corresponding to the phosphoERK staining, was processed in FIJI using the rolling ball background subtraction (ball size 100 pixels) to create a background image. Background images from multiple fields of views were averaged to create an image of the illumination function of the microscope. Each Alexa555 image was then divided by this illumination image using the Cell Profiler plugin "Correct illumination apply" to correct for illumination defects.

To score phosphoErk-positive cells, selected phosphoERK and DAPI images from individual wells were processed in batch using a custom Cell Profiler pipeline. The DAPI channel was segmented to identify cell nuclei. The segmented nuclei were used to seed a second segmentation of the phosphoERK stained channel (Figure S2A). Thresholding parameters for the phosphoERK channel were set using images of PMA stimulated cells, unstimulated cells, and cells labeled with secondary only (for background fluorescence). Segmented nuclei were then related to the segmented phosphoERK objects to score nuclei as phosphoERK positive or negative (e.g., nuclei associate with or without a phosphoERK object). Due to the presence of small phosphoERK positive foci in a portion of cells (found in a fraction of cells even without ligand stimulation), we stipulated that phosphoERK segmented object had to have a minimum size (a minimum diameter of 20 pixels, Figure S2A). This selected for a phosphoERK staining that had an equivalent size and morphology to the DAPI stain, and was equivalent to the phosphoERK staining morphology of PMA-stimulated cells. In general, between 2500-5000 cells were analyzed per well. Positive and negative phosphoERK nuclei were summed across

images from the same well. In Figures 2B and 2C each data point represents the mean from one experiment, where each ligand density was measured in triplicate (Mean $\pm$ SD; n = 3).

Quantification and Analysis of Single Ligand-Receptor Dwell Time

Single molecule diffraction limited spots in the far-red channel were detected and tracked using the FIJI plugin "Trackmate." Ligand dwell times, as computed from the track duration, were fit to a single exponential decay in Prism Graphpad software to calculate τ_{obs}, the mean observed dwell time. The dwell times for the four 11-mer mutant oligonucleotides with increasing G/C content were tested on the one experimental day. Per each experiment, single molecule measurements were made from between 8–12 cells per DNA ligand. Bleach rates were determined by absorbing His10-CLIPf-ybbr13-Atto647N to clean glass imaged using identical illumination and acquisition conditions, and were obtained on the same day as ligand dwell time measurement. Bleaching data for single molecules was processed and analyzed in an identical manner to ligand dwell time data to determine the rate of bleaching (τ_{bl}) (see also Figure S2). τ_{obs} is a combination of the rate of dissociation and photobleaching, and can be corrected to obtain τ_{corr} using the following formula:

$$\tau_{corr} = \left(\tau_{obs}^{-1} - \tau_{bl}^{-1} \right)^{-1}$$

Hidden Markov Model Analysis of Receptor-Ligand Cluster Assembly and ZAP70 Recruitment

The number of fluorescent ligands in a cluster is well described by a Markov process - that is, a stochastic process of ligand addition (i.e., the binding rate) and rates of ligand "removal" (i.e., the combination of the unbinding and the bleaching rate). Therefore, we applied Hidden Markov Model methods to analyze the Atto647N channel data (as described in Figure S3). We implemented this analysis in MATLAB by using the software vbFRET (available at http://vbfret.sourceforge.net/ accessed on September 2015). First the intensity time-series of each tracked cluster was extracted from the coordinates generated by TrackMate. We also extracted the intensity values from the five frames that preceded the appearance of the object (to accurately sample background (i.e., no ligand) intensity values). The fluorescence intensity for each tracked microcluster from a cell was then concatenated to create an ensemble time series which was analyzed by the vbFRET software package, which identified the rates of ligand binding and unbinding (or bleaching) and the fluorescence distributions for cluster composed of n = 1,2,3… ligands. Finally vbFRET reconstructed the time-series of ligand number for each cluster using the Viterbi algorithm. We manually verified the reconstruction for every cluster in each cell, manually correcting for overfitting (i.e., the assigning of multiple Markov Model states to what is manually identifiable as a single fluorescence-intensity state). To assay for the robustness of this analysis to experimental noise we used inverse transform sampling to re-noise a time-series of ligand number from an analyzed experimental dataset. This procedure randomly samples the fluorescence-intensity distribution identified by vbFRET from the experimental data, and ensures the reconstructed data accurately reflects the experimental noise (Figure S3D).

The same analysis protocol was implemented in the ZAP70 channel with minor differences (Figure S3E). The tracking output of bound ligand coordinates was used to pull out the equivalent fluorescence intensity in the ZAP70-mEGFP channel using a custom written MATLAB script. To aid analysis of the ZAP70-GFP signal, we analyzed intensity values extracted from the ZAP70-GFP channel after a rolling ball background subtraction (performed in FIJI with ball size of 3 pixel) in parallel to the raw intensity values. HMM analysis of the ZAP70 data served as a guide for a subsequent careful manual analysis of the data. Manual verification was used to confirm positive recruitment as a puncta of ZAP70-GFP that co-localized and co-migrated with an object in the ligand channel (Figure S3F).

## DATA AND SOFTWARE AVAILABILITY

The custom C code used to analyze the stochastic signaling model is available online (https://github.com/kabirhusain/mjtayloretal_clustergillespie).

ADDITIONAL RESOURCES

Plasmids encoding DNA-CARζ and DNA-CAR$_{TCR}$ have been deposited with Addgene.
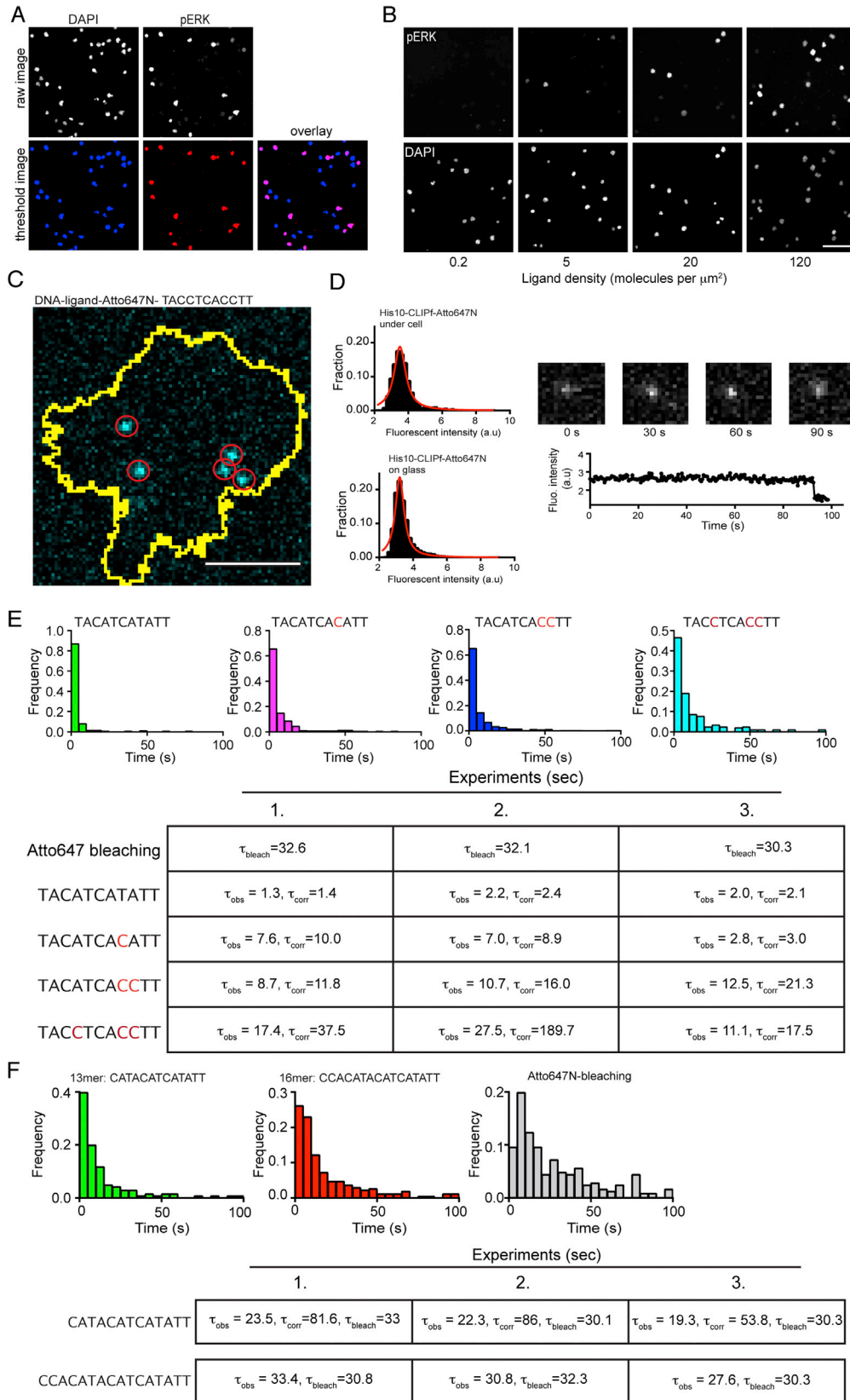An earlier version of this work was previously posted as a preprint on BioRxiv (http://dx.doi.org/10.1101/062877).
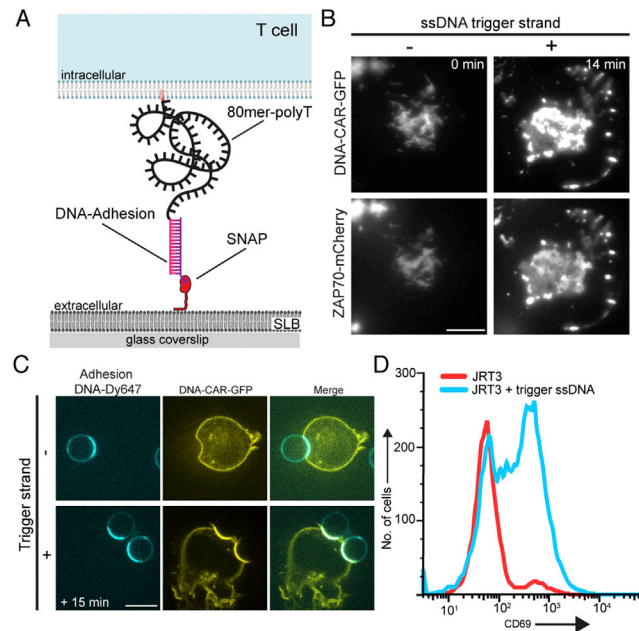
Figure S1. A Triggerable DNA-CARζ System Induces Formation of ZAP70-Positive Microclusters and CD69 Cell-Surface Expression, Related to Figure 1

(A) A schematic of an inert adhesion system for tethering Jurkat T cells to supported lipid bilayers, using the method of Selden et al. (Selden et al., 2012). The 5′ end of the DNA adhesion strand has a covalently bound lipid, which enables insertion into the plasma membrane. The 80 nucleotide polyT linker is depicted as compacted entropic spring, which is consistent with measurements of the persistence length of polyT ssDNA (Murphy et al., 2004). Tethering occurs through a 20 nucleotide segment of the adhesion strand that base pairs with a complementary region of the DNA strand conjugated to His10-CLIPf protein on the supported lipid bilayer (SLB). We do not know the precision dimensions of the adhesion strand and it is likely able to adopt many conformations. However, the glycocalx surrounding most cells is 20 nm or larger and the adhesion strand must extend beyond this distance for sufficiently long periods of time, so as to irreversibly hybridize with complementary sequences on the SLB. The glycocalx barrier is likely to explain why linker lengths of 40-60 nucleotides are needed for effective cell-cell adhesion using DNA (Selden et al., 2012). We also do not think that the adhesion strand results in very close apposition of the two cell membranes (e.g., < 15 nm). Recent work by Chang et al. (Chang et al., 2016) showed that close contact of the T cell with another surface results in CD45 exclusion and TCR-independent signaling, which we do not see for T cells contacting bilayers with the DNA adhesion system alone; addition of the ligand-receptor strands is required for this behavior.

(B) Formation of ZAP70-mCherry-positive microclusters and cell spreading after addition of DNA trigger strand, which results in an overlap of 36 bp. Bar, 5 μm. Time after addition of the trigger DNA strand is shown.

(C) JRT3 cells expressing the DNA- CARζ-GFP were mixed with 7 μm silica microspheres with adsorbed supported lipid bilayers functionalized with a DNA adhesion strand (in this example, conjugated to His10-SNAPf-ybbr13-Dy647) and DNA ligand (conjugated to His10-CLIPf)). SLB were set up on silica micro-sphere to maintain cells in suspension and facilitate FACS analysis. Cells and beads were mixed in a 96-well plate before the addition of the DNA trigger strand. To check SLB formation on silica beads as well as DNA- CARζ activation, a portion of cells were plated onto poly-L-lysine coated coverslips and imaged by spinning disk confocal microscopy. Bilayer fluidity was checked by the enrichment of the His10-SNAPf-Dy647 at the cell-bead interface. Fifteen minutes after addition of trigger strand, the DNA- CARζ-GFP is enriched at the cell-microsphere interface. Scale bar, 10 μm.

(D) Four hours after addition of trigger DNA strand, cells were stained for CD69 and analyzed by FACS. CD69 expression was upregulated on the cell surface for cells that were incubated with trigger strand (blue trace) compared with control cells (red trace).

A

DAPI   pERK

raw image

threshold image   overlay

B

pERK

DAPI

0.2   5   20   120

Ligand density (molecules per μm²)

C

DNA-ligand-Atto647N- TACCTCACCTT

D

His10-CLIPf-Atto647N under cell

0 s   30 s   60 s   90 s

His10-CLIPf-Atto647N on glass

E

TACATCATATT   TACATCACATT   TACATCACCTT   TACCTCACCTT

	Experiments (sec)		
	1.	2.	3.
Atto647 bleaching	τ_{bleach}=32.6	τ_{bleach}=32.1	τ_{bleach}=30.3
TACATCATATT	τ_{obs} = 1.3, τ_{corr}=1.4	τ_{obs} = 2.2, τ_{corr}=2.4	τ_{obs} = 2.0, τ_{corr}=2.1
TACATCACATT	τ_{obs} = 7.6, τ_{corr}=10.0	τ_{obs} = 7.0, τ_{corr}=8.9	τ_{obs} = 2.8, τ_{corr}=3.0
TACATCACCTT	τ_{obs} = 8.7, τ_{corr}=11.8	τ_{obs} = 10.7, τ_{corr}=16.0	τ_{obs} = 12.5, τ_{corr}=21.3
TACCTCACCTT	τ_{obs} = 17.4, τ_{corr}=37.5	τ_{obs} = 27.5, τ_{corr}=189.7	τ_{obs} = 11.1, τ_{corr}=17.5

F

13mer: CATACATCATATT   16mer: CCACATACATCATATT   Atto647N-bleaching

	Experiments (sec)		
	1.	2.	3.
CATACATCATATT	τ_{obs} = 23.5, τ_{corr}=81.6, τ_{bleach}=33	τ_{obs} = 22.3, τ_{corr}=86, τ_{bleach}=30.1	τ_{obs} = 19.3, τ_{corr}= 53.8, τ_{bleach}=30.3
CCACATACATCATATT	τ_{obs} = 33.4, τ_{bleach}=30.8	τ_{obs} = 30.8, τ_{bleach}=32.3	τ_{obs} = 27.6, τ_{bleach}=30.3

(legend on next page)

Figure S2. PhosphoErk Quantification and Measuring Receptor-Ligand Dwell Time, Related to Figure 2 and STAR Methods

(A) A customized Cell Profiler analysis pipeline was used to process phosphoERK staining images and score JRT3 cells as phosphoERK positive or negative. First the DAPI channel raw images were segmented to identify the nucleus (shown as blue in the threshold image). Second the raw images of the phospoERK staining channeled were segmented using thresholding parameters set with control datasets (PMA stimulated cell, non-stimulated cells, and cells stained with secondary antibody only). Identified phosphoERK nuclei are shown as red in the thresholded image. Cells were scored phosphoERK positive when a DAPI nucleus overlapped with a segmented phosphoERK nucleus. A minimum threshold area was set for the nucleus as described in the STAR Methods. In the overlay of the thresholded DAPI and phosphoERK images the nuclei scored positive appear magenta. Scale bar, 100 μm.

(B) Raw and threshold phosphoErk and DAPI images presented in Figure 2A. Scale bar, 100 μm.

(C) JRT3 cells expressing DNA-CARζ were imaged using a two-camera TIRF microscope with simultaneous excitation of DNA- CARζ-GFP and DNA-ligand-Atto647N. A long 500 ms exposure in the Atto647N channel revealed single molecules (red circles) of DNA-ligands-Atto647N detected at the SLB-cell interface (yellow outline, obtained by segmentation using DNA- CARζ-GFP fluorescence). In contrast to bound DNA ligand, unbound DNA ligands diffuse more rapidly and appear as an unresolved fluorescent blur in images taken at 500 ms exposure. (See method of O'Donoghue et al.[O'Donoghue et al., 2013.) Scale bar, 2.5 μm.

(D) Top, mean fluorescence intensities of single receptor-bound DNA ligands versus single His10-CLIPf-ybbr labeled with Atto647N absorbed to glass and imaged with identical conditions. Bottom, representative intensity trace of a single receptor-bound DNA ligand labeled with Atto647N which is bound for 90 s, before disappearing by single step photobleaching/unbinding.

(E and F) Histograms of dwell times for DNA ligand and tables of individual dwell times (τ_{obs}) and Atto647N bleaching measurements (τ_{bl}). Panel c shows the 3 experiments that make up the average dwell times presented in Figure 2D for the 11-mer DNA ligands. Each experiment for the 11-mer ligand represents measurement conducted on one experimental day. A single experiment consisted of single molecule dwell times measurement from > 10 cells with 300–700 single receptor-ligand binding events per DNA ligand analyzed. Histograms of individual dwell time measurements for the 13-mer and 16-mer DNA ligand are presented in panel (D). The τ_{obs} was corrected using the bleaching measurement performed during each experiment to obtain an estimate of average dwell time (τ_{corr}) of receptor-ligand unbinding from:

$$\tau_{corr} = \left(\tau_{obs}^{-1} - \tau_{bl}^{-1} \right)^{-1}$$

This method to estimate τ_{corr} is most accurate when τ_{obs} is considerably smaller that τ_{bl}. Measurements of τ_{obs} that approach τ_{bl} have an inflated τ_{corr}, as is the case the 11-mer ligand with the greatest G/C content (AAGGTGAGGTA). In the case of the 16-mer DNA ligand, τ_{obs} is equivalent to τ_{bl} making this correction method more prone to error.
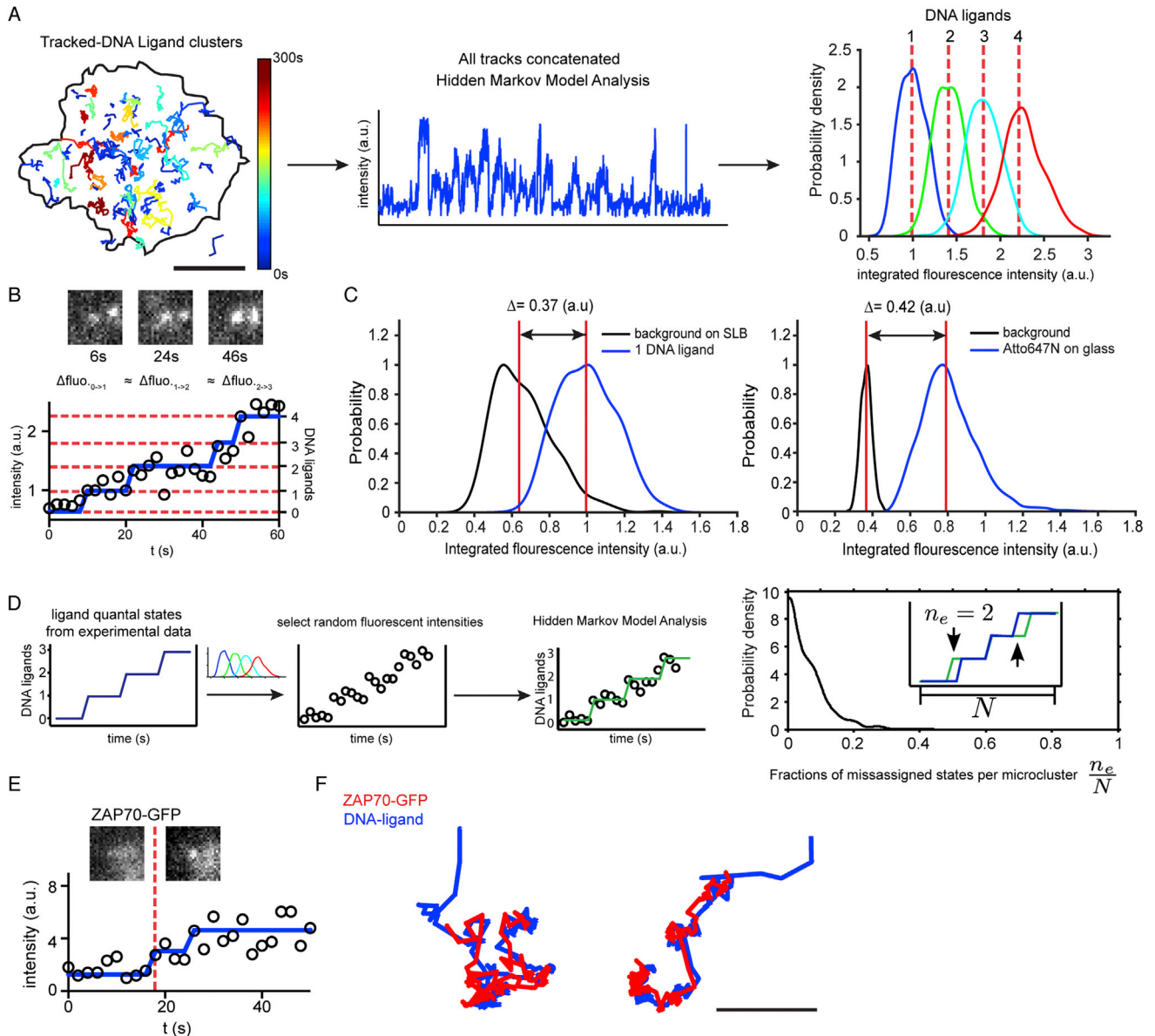
Figure S3. Analysis of Receptor-Ligand Microcluster Formation and ZAP70 Recruitment, Related to Figure 3 and STAR Methods

(A) We adapted a previously described (Bronson et al., 2009) Hidden Markov Model (HMM) analysis to identify the number of fluorescent ligands in each frame from the fluorescence intensity of tracked Atto647N ligand clusters. The intensity time-series of each tracked cluster was extracted from the coordinates generated by TrackMate. Shown is an example of 86 particle trajectories detected at the cell-SLB junction for the 16-mer DNA ligand at ∼1 molecule/μm² (black outline, segmented cell boundary; microcluster trajectories color coded by lifetime). Bar, 5 μm. The intensity time-series of all tracks were then concatenated, and the ensemble intensity time series was analyzed by a statistical maximum evidence approach, implemented with a variational Bayesian method. This analysis identified the rates of ligand addition and removal and the fluorescence distributions associated with n = 1,2,3... bound ligands from the intensity data. We found the assigned distributions of fluorescence intensities are overlapping, as is expected from the highly fluctuating background noise generated by the fluorescent blur of the rapidly-diffusing unbound Atto647N-ligand on the camera detector. Nonetheless, each distribution shows a clear maximum and does not exhibit any structure indicative of misfitting (e.g., multiple peaks). Furthermore, the difference in the medians of each distribution peak is quantized, commensurate with the fluorescence intensity arising from a discrete numbers of fluorescent molecules. The identified rates and fluorescence distributions were used to reconstruct the time-series of ligand number for each cluster. This resulted in the identification of the step changes in the fluorescent signal that denoted new ligand-binding events.

(B) Example DNA ligand intensity time series overlaid with HMM-assigned ligand number at each time point (blue trace). The step changes in the blue trace represent the binding of new ligands. The dashed red lines represent the median fluorescence intensity from n = 1,2,3… fluorescent ligands (derived from the fluorescence intensity distributions shown in A).

(C) To ensure that the states identified by the HMM analysis corresponded to quantized intensity values characteristic of single molecules, we performed an identical analysis on datasets consisting of single Atto647N fluorophores stuck to glass slides. We then compared the fluorescent distributions of the n = 0 (i.e.,

background) and n = 1 fluorophore number with the distributions of the n = 0 and n = 1 fluorescent ligands found in the cell-bilayer data. We find that the difference in their medians is in good agreement (3.7 versus 4.2 fluorescence intensity units), confirming that the HMM analysis is reliably identifying states corresponding to discrete numbers of fluorescent molecules. We note that the HMM analysis was able to correctly identify states in both the stuck Atto647N dataset as well as the cell-based data-set despite the differences in noise between them (compare the distribution in the background on a SLB versus a glass slide). The background fluorescence intensity of the SLB was measured by sampling 5 time points previous to cluster appearance in a region of interest centered on the coordinate where the tracked microcluster appeared. The background distribution of the glass slide was obtained by randomly sampling regions in the image stack not occupied by single molecules.

(D) We assayed for the robustness of the HMM analysis to the broad fluorescence distributions by constructing a computer-generated dataset. Time series of ligand binding and unbinding/bleaching were taken from an analyzed experimental dataset and converted into fluorescence values by sampling from the experimentally intensity distributions for n = 1,2,3… DNA ligands shown in panel (a). This ensured that the noise and the transition rates between states in the computer-generated dataset were reflective of experimentally collected data. The resultant time-series were analyzed and the HMM reconstruction of state time series was compared to the original values. The error was quantified as the fraction of time-point in a time-series in which the HMM reconstruction misidentified the state. Plotting the distribution of error confirms that the algorithm is able to identify states with < 10% error despite the noise present experimentally.

(E) We used the algorithm described in (A) conservatively to assay for presence or absence of ZAP70. Due to the noisy background signal associated with the cytosolic ZAP70-GFP, we checked the HMM assignment of the first ZAP70-GFP binding event by manual visual inspection to determine whether the detected step change in intensity represented recruitment.

(F) Representative DNA-ligand microclusters trajectories (blue) overlaid with the trajectory of an associated ZAP70-GFP spot (red). Positive ZAP70 recruitment was defined as a puncta of ZAP70-GFP that co-localized and co-migrated with an object in the ligand channel. By inspection of the data we found misidentified ZAP70 recruitment arose from two factors: (1) fluctuation in the Z axis of the cell in the evanescent field, and (2) the presence of intracellular structures (likely endosomes) that were ZAP70-GFP positive that were prominent in some cells. These ZAP70-GFP punctae did not colocalize or move with ligand-bound re-ceptors. Bar, 1 μm.
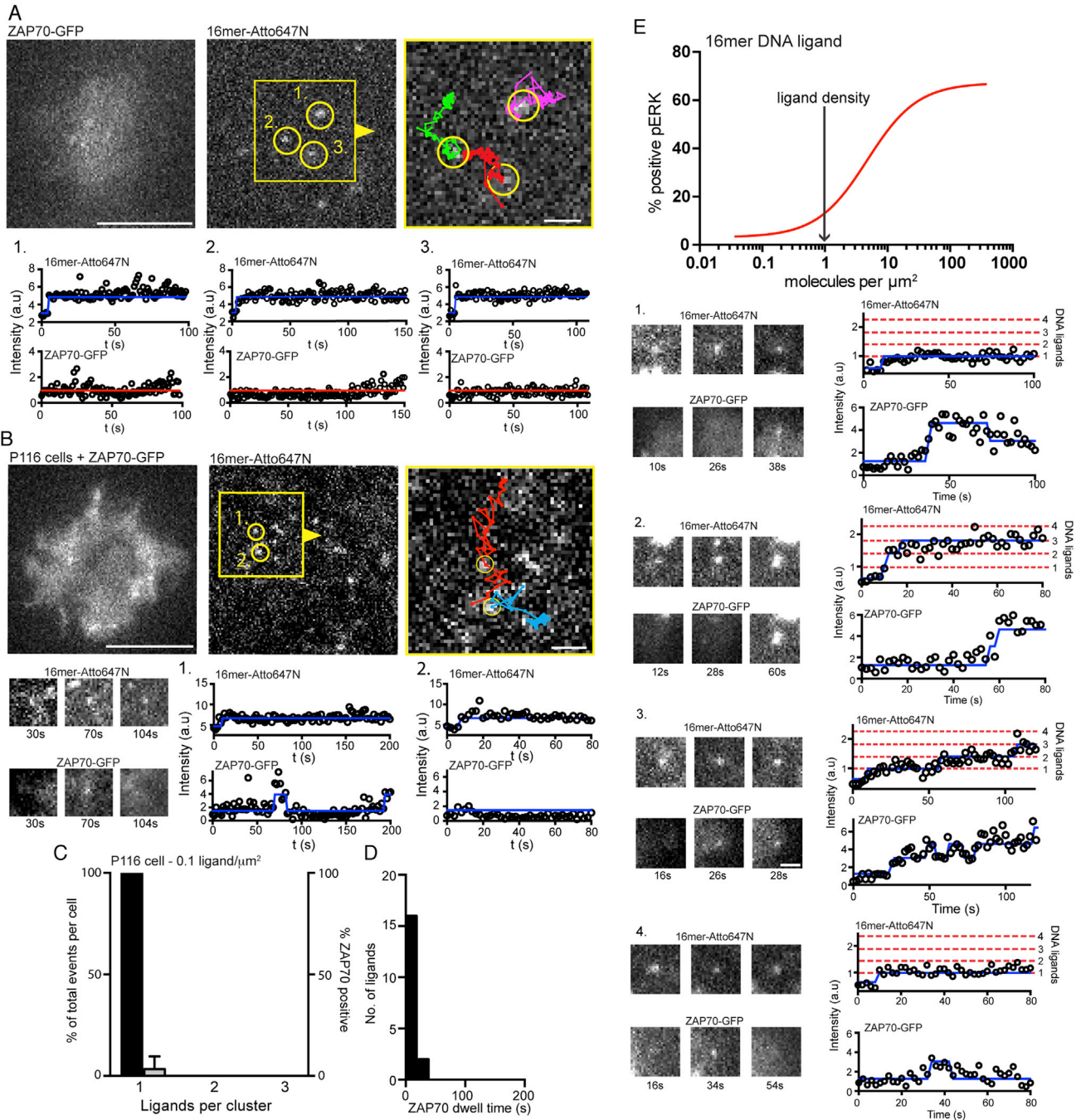
Figure S4. Gallery of Single-Molecule Binding Events in JRT3 and P116 (ZAP70-Negative Jurkat Cell Line) Expressing DNA-CARζ and ZAP70-GFP, Related to Figure 3

Single-molecule imaging was performed at a density 0.1 16-mer-DNA ligands/ μm².

(A) TIRF images of 16-mer DNA ligands labeled with Atto647N. Single bound ligands are marked by yellow circles in region of interest (red box and arrowhead). Bar, 5 μm. Right panel, region of interest overlaid with the tracked single molecule trajectories. ROI bar, 1 μm. Bottom panels, the fluorescence intensity time series for the single molecules of Atto647N labeled 16-mer ligand and the corresponding ZAP70-GFP fluorescence intensity. Fluorescence-intensity time series for ligand and ZAP70 channels analyzed as described in Figure S3.

(B) TIRF images of a P116 cell expressing ZAP70-GFP and DNA- CARζ. Bar, 5 μm. Region of interest (yellow box and arrowhead) on right overlaid with single molecule trajectories. ROI bar, 1 μm. Fluorescence-intensity plots for bound ligands shown below images.

(C) Quantification of ZAP70 recruitment to single bound receptors in P116 cells. Shown are the number single bound ligand-receptor pairs (percent of total, black bars) and the percent of single bound receptor and clusters that recruited ZAP70-GFP (gray bars) in P116 Jurkat cells. ZAP70 recruitment was only observed in 2.2% ± 4% of single-molecule events in P116 cells. Results are mean ± SD from 6 cells for P116 Jurkat cells.

(legend continued on next page)

(D) Quantification of ZAP70 dwell time at single bound ligands of 16-mer DNA ligand in P116 cells (n = 18).

(E) Gallery of examples showing formation of receptor-ligand microclusters and ZAP70 recruitment to a high-affinity 16-mer DNA ligand acquired by at a density of 1 ligands/μm^2. The DNA ligand and ZAP70 fluorescence-intensity time series were analyzed as described in Figure S3. Receptor-ligand microclusters of 16-mer DNA-ligand that formed in the initial 5 min of interacting with the SLB. Although uncommon, ZAP70 recruitment was observed at single molecules of bound 16-mer ligand (examples 1–3). In some cases ZAP70 recruitment to single bound 16-mer ligands was transient (example 4). Receptor-ligand microclusters consisting of 2 or more 16-mer DNA ligands (example 2) were more likely to recruit ZAP70. Bar, 1 μm.
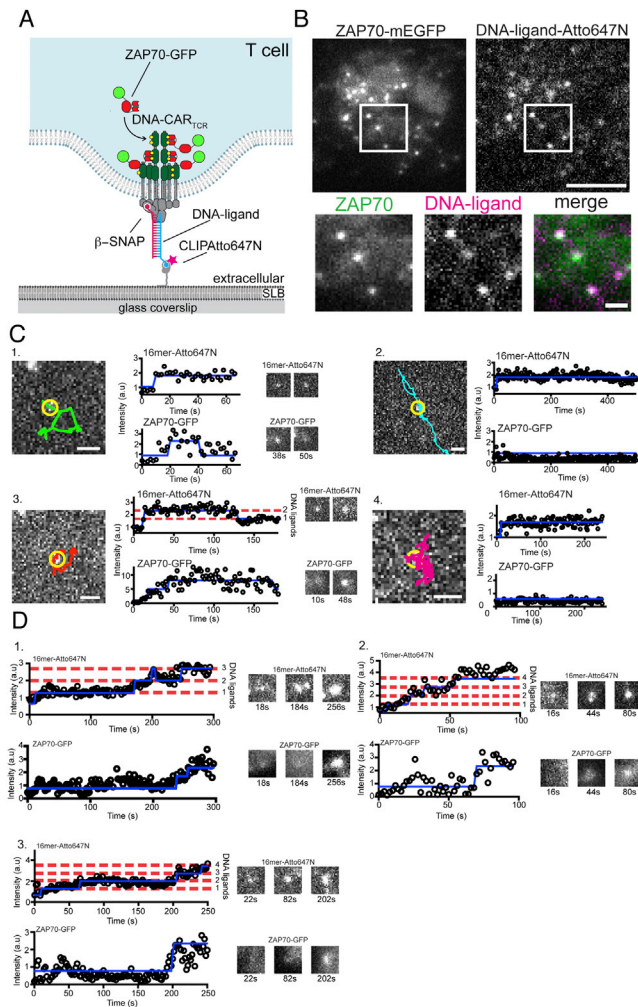
Figure S5. Recruitment of ZAP70 to DNA-CAR$_{TCR}$ Microclusters and Galleries of DNA-CAR$_{TCR}$-Binding Events of 0.1 and 1 16-mer-DNA Ligands/μm^2, Related to Figure 4

(A) Schematic of the DNA-CAR$_{TCR}$. The SNAPf tag was fused to the extracellular domain of the TCRβ and expressed in JRT3 cells (TCRβ-negative) to reconstitute the full TCR.

(B) TIRF microscopy images of a JRT3 Jurkat cell expressing ZAP70-GFP and DNA-CAR$_{TCR}$ labeled with 16-mer ssDNA after landing on a SLB with a complementary 16-mer strand (120 molecules per μm^2). Microclusters of ligand-receptor complexes formed within ~2 min and recruited ZAP70-GFP (inset). Scale bar, 5 μm; inset scale bar, 1 μm.

(C) Gallery of single-molecule binding event at a density 0.1 16-mer-DNA ligands/ μm^2. Left panels, TIRF images of 16-mer DNA ligands labeled with Atto647N (yellow circle) and overlaid with the tracked single-molecule trajectories. Right panels, the fluorescence-intensity time series for the single molecules of Atto647N labeled 16-mer ligand and the corresponding ZAP70-GFP fluorescence intensity. Fluorescence-intensity time series for ligand and ZAP70 channels were analyzed as described in Figure S3. Although uncommon, transient ZAP70 recruitment was observed at some single ligands bound to DNA-CAR$_{TCR}$ (example 1). Example 3 shows a rare example of a small cluster consisting of two ligands forming, which also recruits ZAP70. Example 2 and 4, show more common single molecules DNA-CAR$_{TCR}$ binding events that showed no discernable ZAP70 recruitment. Scale bar, 1 μm.

(D) Examples of DNA-CAR$_{TCR}$ receptor-ligand microcluster formation and ZAP70 recruitment to a high affinity 16-mer DNA ligand. Data shown were acquired by at a density of 1 ligands/μm^2. The DNA ligand and ZAP70 fluorescence-intensity time series were analyzed as described in Figure S3. DNA-CAR$_{TCR}$ receptor-ligand microclusters of 16-mer DNA-ligand that formed in the initial 5 min of interacting with the SLB.
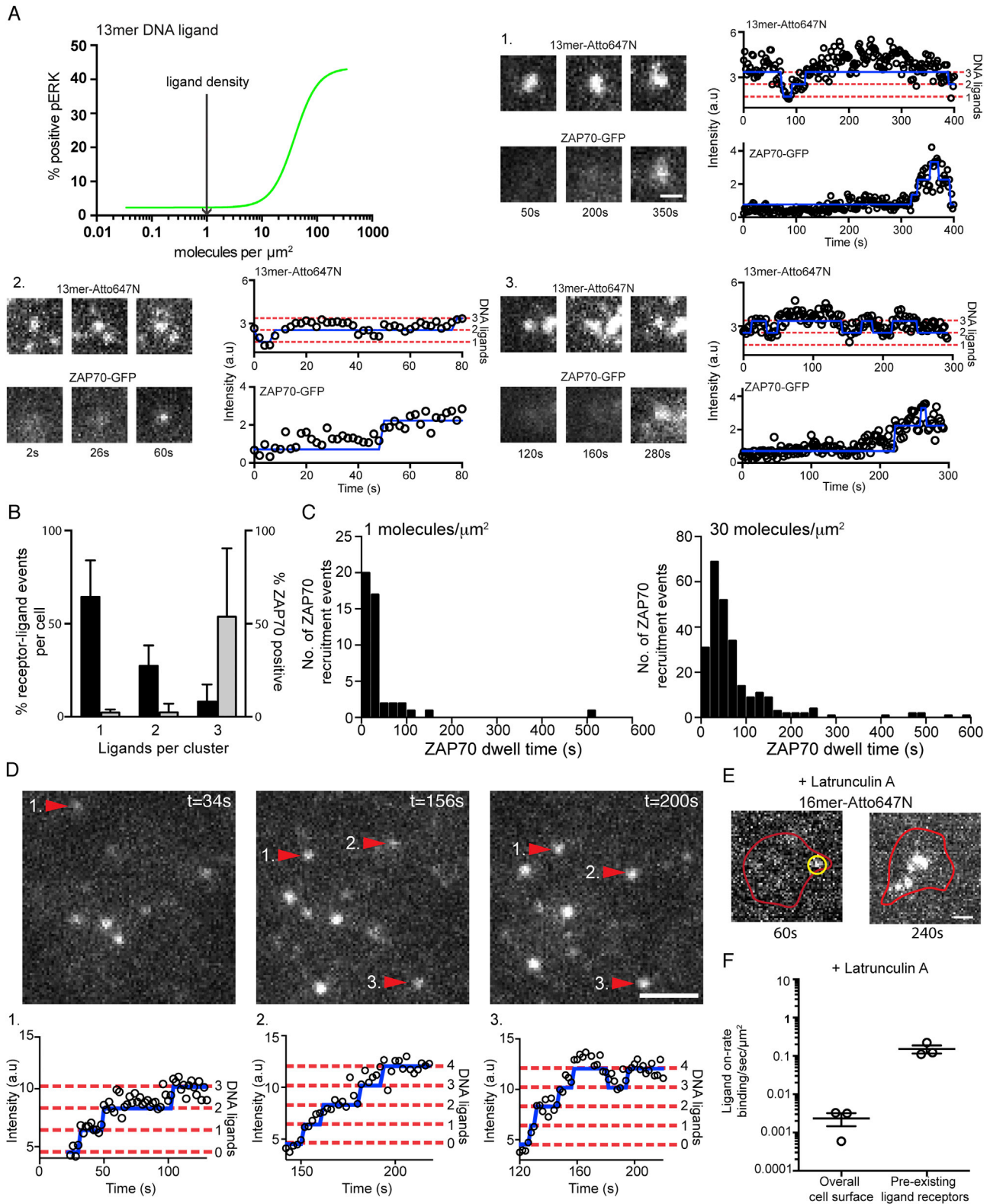
Figure S6. Receptor-Ligand Microcluster Formation and ZAP70 Recruitment to a Low-Affinity 13-mer DNA Ligand, Related to Figures 5 and 6
13-mer DNA ligand data shown acquired at a density of 1 ligands/μm². The DNA ligand and ZAP70 fluorescence-intensity time series were analyzed as described in Figure S3.

(legend continued on next page)

(A. A gallery of examples showing the formation of small receptor-ligand microclusters of 13-mer DNA ligand observed after cells had interacted SLBs for > 15 min.

(B) Quantification of ZAP70 recruitment and dwell time to ligand-receptors of 13-mer DNA ligand. Bar plot shows the number single bound ligand-receptor and clusters (percent of total binned, black bars) and quantification of (percent of total that recruit ZAP70, gray bars). Single molecule ligand binding events and receptor-ligand clusters of increasing ligand number that persisted for at least 30 s were scored for whether they recruited ZAP70-GFP. The initial point of ZAP70 recruitment was referenced to the number of ligands within the receptor-ligand spot. 53% $\pm$ 37% of receptor-ligand clusters containing 3 or more ligand recruit ZAP70 compared to 2% $\pm$ 1.7% of single bound ligands. Results are mean $\pm$ SD from n = 4 cells.

(C) The distribution of ZAP70 dwell times at receptor-ligand clusters at 1 ligands/μm^2 (n = 46 clusters from 4 cells) and 30 ligands/μm^2 (N = 276 cluster from 4 cells). Formation of DNA-CAR$_{TCR}$ microclusters from single ligand-receptor binding events (D and E).

(D) A TIRF image of DNA-CAR$_{TCR}$ -bound 16-mer DNA ligand organized into receptor-ligand clusters that grow by adjacent ligand binding events (red arrows numbered 1–3). Bar, 2.5 μm. Clusters grow by sequential addition of newly bound ligand; the blue line overlaid the fluorescence intensity represents detected step changes in fluorescence intensity (see STAR Methods and Figure S3).

Formation of DNA receptor-ligand clusters in the presence of latrunculin A (E and F).

(E) TIRF images showing cluster formation nucleated from a single bound receptor (yellow circle) in the presence of latrunculin A (1 μM) with a 16-mer at 1 ligands/μm^2 (red outline show the cell outline obtained by segmentation using the ZAP70-GFP fluorescence). Bar, 1 μm.

(F) The rate of new ligand binding events near to an existing receptor-bound ligand (quantal increase in intensity in an existing diffraction-limited spot) or outside of these zones (measured by the sudden appearance of a new bound ligand in the contact area between the cell with the supported lipid bilayer) in cell treated with latrunculin A (1 μm). The ligand-receptor on-rate was expressed as the number of events per sec per μm^2 membrane surface area (using 0.126 μm^2 for a diffraction limited spot of a pre-existing ligand-receptor pair). Shown is the mean $\pm$ SEM from 3 cells.
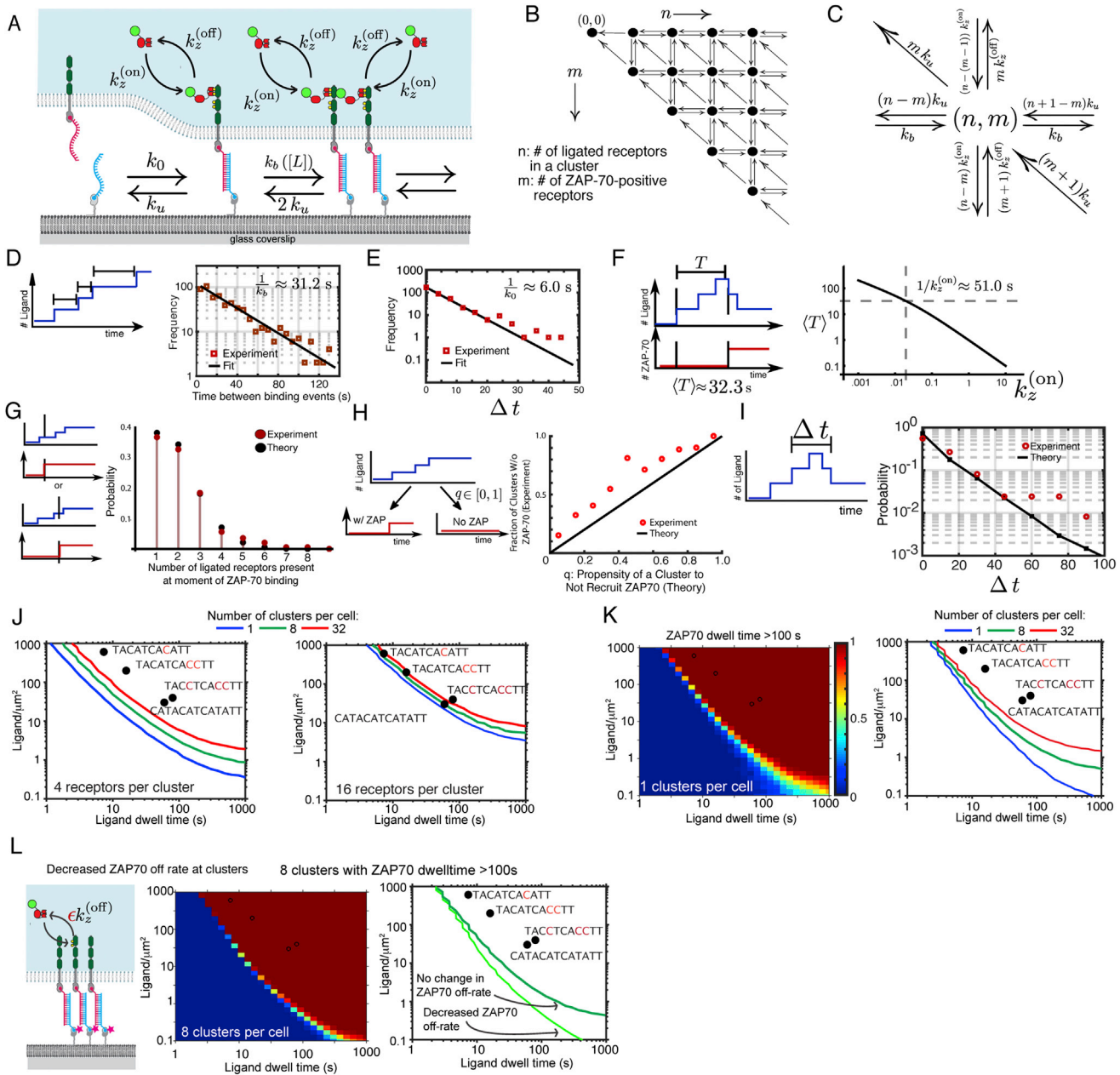
Figure S7. Construction of a Theoretical Signaling Model, Related to Figure 7

(A) Schematic of the model, showing contact site formation (with rate k_0), maturation into a cluster by additional ligand binding (with rate k_b), ZAP70 binding and unbinding, and ligand unbinding.

(B) State space of an individual cluster. Each state is identified by the doublet of integers (n, m): the number of ligated receptors (n) and the number of those receptors that are ZAP70 positive (m). Note that $m \leq n$.

(C) Possible stochastic transitions, and associated rates, from a representative state (n, m).

Estimation of model parameters from experimental data:

(D) Parameter k_b: Histogram of waiting times between ligand binding at a cluster (red squares—621 binding events over 434 tracked ligand clusters from 14 cells) with an exponential fit (black line) with rate constant k_b. Left: schematic of measurement.

(E) Distribution of waiting times between appearances of ligand tracks, (381 waiting times from 14 cells). In red is an exponential fit with rate k_0.

Validation of model against data:

(F) Parameter $k_z^{(on)}$: Left: Schematic of measurement of the average time to first ZAP70 recruitment, < T > . Value obtained from 197 ZAP70 recruitment events from 14 cells. Right: < T > as a function of the ZAP70 on-rate, obtained from the model, with dashed lines indicating experimentally observed value (horizontal line) and corresponding rate (vertical line).

(legend continued on next page)

(G) Statistics of ZAP70 recruitment to clusters of ligated receptors, i.e., number of ligands present in cluster at the moment of the first ZAP70 recruitment event, for both theory (black) and experiment (red - from 197 ZAP70 recruitment events).

(H) Ligand tracks from experimental data (428, from 14 cells) binned by their propensity to not recruit ZAP70 (see text for details of calculation), compared with the fraction of each bin that do not, in fact, recruit ZAP70. Small but consistent deviation of data (red circles) from theoretical prediction (black line) indicates that less ZAP70 is seen experimentally than expected from the model.

(I) "Lifetime" of a cluster, defined as n > 1 (see inset), for the 13-mer ligand (black circles) against simulation (red squares and line). Simulation was performed with the bleaching-included ligand off-rate of $20\,s^{-1}$. Note that the first four bins contain the majority of the experimental data (114 of 129 data points), with the last few bins containing 1 to 3 data points each.

(J–L) We quantitatively assessed the theoretical signaling model by performing stochastic simulations of cells interacting with a ligand functionalised supported lipid bilayer. These simulations were performed over a range of ligand densities (.01 to 1000 molecules per μm^2) and ligand affinities (off-times of 1 to 1000 s) for a fixed time interval of 500 s. At each point in this parameter space we simulated 250 cells. The output of this simulation was time-series data of ligand binding, cluster formation and ZAP70 recruitment. We analyzed this time series data for when clusters appeared with a particular number of ZAP70 positive receptors or ZAP70 association times.

(J) The number of ZAP70 receptors per cluster was used to define potential activation criteria. In example given the activation criteria is defined as the formation of a receptor-ligand cluster that have 4 or 16 or greater ligands. Colored lines indicated the 20% contour from probability heatmaps of when > 20% of simulated cells forming the indicated number of clusters with a minimum of 4 or 16 ZAP70-positive receptors. To compare the predicted emergence of these features in the simulated data with experimental data, we plotted the ligand densities and ligand dwell time at which the indicated DNA ligands elicited a response of 20% pERK-positive cells (Figures 2 and S2).

(K) Analysis of when clusters form with a ZAP70 association time of 100 s. Left, heatmap showing the probability of 1 cluster forming with a ZAP70 dwell time of 100 s. Right, colored lines indicated the 20% contour from probability heatmaps of when > 20% of simulated cells forming the indicated number of clusters with a ZAP70 dwell time of > 100 s.

(L) Schematic of a modified model in which the ZAP70 off rate is decreased at a cluster of ligated receptors ($\varepsilon<1$, see SI text for details) and heatmap showing the results of simulation. Comparison of this model with a decreased dwell time of ZAP70 to the standard model, shows that decreased off rate of ZAP70 increases the probability of ZAP70 recruitment to high-affinity ligand at lower ligand densities.